Journal of Marine Systems 163 (2016) 61–79

Contents lists available at ScienceDirect

Journal of Marine Systems

journal homepage: www.elsevier.com/locate/jmarsys

Characterizing the surface circulation in Ebro Delta (NW Mediterranean) with HF radar and modeled current data

P. Lorente [a,*], S. Piedracoba [b], M.G. Sotillo [a], R. Aznar [a], A. Amo-Balandron [a], A. Pascual [a], J. Soto-Navarro [a], E. Alvarez-Fanjul [a]

[a] Puertos del Estado, Avenida del Partenón 10, 28042 Madrid, Spain
[b] University of Vigo, Marcosende s/n, 36310 Vigo, Pontevedra, Spain

ARTICLE INFO

Article history:
Received 28 February 2016
Received in revised form 4 June 2016
Accepted 1 July 2016
Available online 02 July 2016

Keywords:
High frequency radar
Coastal circulation
Model skill assessment
Skill metrics
Operational oceanography

ABSTRACT

Quality-controlled current observations from a High Frequency radar (HFR) network deployed in the Ebro River Delta (NW Mediterranean) were combined with outputs from IBI operational ocean forecasting system in order to comprehensively portray the ocean state and its variability during 2014. Accurate HFR data were used as benchmark for a rigorous validation of the Iberia-Biscay-Ireland (IBI) regional system, routinely operated in the frame of the Copernicus Marine Environment Monitoring Service (CMEMS). The analysis of skill metrics and monthly averaged current maps showed that IBI reasonably captured the prevailing dynamic features of the coastal circulation previously observed by the HFR, according to the moderate resemblance found in circulation patterns and the spatial distribution of eddy kinetic energy. The model skill assessment was completed with an exploration of dominant modes of spatiotemporal variability. The EOF analysis confirmed that the modeled surface current field evolved both in space and time according to three significantly dominant modes of variability which accounted for the 49.2% of the total variance, in close agreement with the results obtained for HFR (46.1%). The response of the subtidal surface current field to prevailing wind regime in the study area was examined in terms of induced circulation structures and immediacy of reaction by performing a conditional averaging approach and a time-lagged vector correlation analysis, respectively. This observations-model synergistic strategy has proved to be valid to operationally monitor the complex coastal circulation in Ebro Delta despite the observed model drawbacks in terms of reduced energy content in surface currents and some inaccuracies in the wind-driven low frequency response. This integrated methodology aids to improve the prognostic capabilities of IBI ocean forecasting system and also to facilitate high-stakes decision-making for coastal management in the Ebro River Delta marine protected area.

1. Introduction

The Ebro River Delta (NE coast of Spain, Fig. 1) is one the largest and most biodiverse aquatic ecosystem in the western Mediterranean Sea. The nearshore deltaic area is experiencing severe erosion and reshape due to both human-induced and natural factors. The former are related to dam constructions in Ebro River hydrographic basin, leading to a drastic reduction of sediment discharge and the subsequent surface loss (Palanques et al., 2002), whereas the latter include a variety of marine processes (i.e., wave action eroding exposed wetlands) impacting on the evolution of the delta coast (Palanques and Guillen, 1998).

The freshwater input of Ebro River together with coastal wind-induced upwelling causes high nutrients concentration, making the Ebro Delta a highly productive area in terms of phytoplankton and zooplankton (Würtz, 2010). Since the biological connectivity between this sensitive marine protected area and adjacent ecological regions constitutes a key issue, a number of researches have been conducted to deduce transport pathways not only for nutrients, larvae and juveniles but also for sediments and pollutants (Zelenke et al., 2009). The spread of chemical and organic contaminants (i.e., agricultural run-off) may impact dramatically on the local ecosystem if the pollutants recirculate near the coast rather than dispersing on the open sea (Coulliette et al., 2007).

The previous considerations underline the necessity of an efficient coastal management in order to promote the conservation and integrity of marine ecosystems. The constant monitoring of coastal waters requires an observing network based on disparate cutting-edge technologies (gliders, satellites, moorings, etc.) that adequately samples the study domain, in conjunction with an ocean circulation numerical

* Corresponding author.
E-mail address: plorente@puertos.es (P. Lorente).

http://dx.doi.org/10.1016/j.jmarsys.2016.07.001
0924-7963/

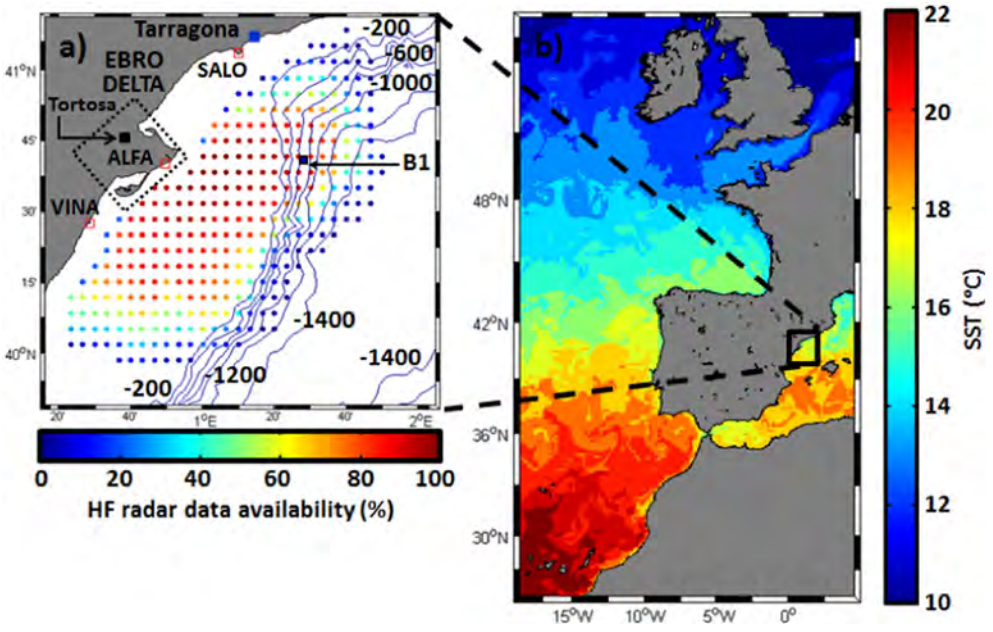

Fig. 1. (a) HFR deployed at the Ebro Delta, composed by three sites (red squares). Colored dots denote the temporal coverage in percent of HFR surface current total vectors for 2014. Isobath depths are labeled every 200 m. Locations of Tarragona buoy (B1) and Tarragona harbour are marked with blue solid squares. Location of Tortosa hydrological station is denoted by a black solid square. (b) Example of an hourly sea surface temperature (SST) map predicted by IBI operational ocean forecasting system. (For interpretation of the references to colour in this figure legend, the reader is referred to the web version of this article.)

model with a proper horizontal resolution to capture all the details of the coastline and the bathymetry (Ngodock et al., 2015).

In this context, a 13.5 MHz CODAR SeaSonde High Frequency radar (HFR) was deployed in December 2013 (Fig. 1, a) to support marine domain awareness and assist decision- and policy-making related to water quality, maritime safety and mitigation of anthropogenic hazards. This remote-sensing land-based technology is being increasingly used worldwide to map the evolving current fields in near real-time over broad spatial areas. HFR estimations can be used for a wide range of practical applications such as harbour management, vessel tracking, search and rescue (SAR) operations and oil spill emergencies (Bellomo et al., 2015), thereby contributing to the global societal benefit. Nowadays, the long-term environmental monitoring of the Ebro Delta is complemented by 3-D outputs from the Iberia-Biscay-Ireland (IBI) operational ocean forecasting system (OOFS). This regional NEMO-based application has been providing continuous daily ocean model estimates and forecasts of currents and other physical parameters for the IBI regional seas (Fig. 1, b) since 2011 (Sotillo et al., 2015), first in the frame of MyOcean projects and later as part of the Copernicus Marine Environment Monitoring Service (CMEMS), which represents a quantum leap in terms of operational capabilities and oceanographic forecasting service at European level.

HFR-derived synoptic surface current maps can be optimally combined with ocean circulation models via data assimilation framework (Iermano et al., 2016; Marmain, 2013; Gopalakrishnan and Blumberg, 2012; Paduan and Shulman, 2004) or blending scheme (Stanev et al., 2015; Lipphardt et al., 2000), whose usefulness has been previously demonstrated. In the present work, the attention is focused on the advantages of using HFR measurements for an in-depth performance evaluation of regional models, as reported in prior studies (Cianelli et al., 2015; O'Donncha et al., 2015; Guihou et al., 2013; Wilkin and Hunter, 2013; Chavanne et al., 2007). HFR estimations improve the model description by resolving low scale processes in areas with significant topographic gradients, whereas model outputs provide a continuous 3-D quantitative picture with vertical resolution that completes the surface radar-derived information when the quality data or the spatiotemporal coverage are poorer. Furthermore, numerical models supplement radar measurements thanks to the provision of predictive products with different forecast horizons. Previous studies in the western Mediterranean Sea have reported the benefits of a multi-disciplinary assessment approach to identify OOFS shortcomings and improve the representation of local physical processes (Juza et al., 2015a, 2015b; Tonani et al., 2009; Maidana et al., 1999).

The integrity of HFR data in the Ebro Delta during 2014 was previously assured by applying a combined quality control methodology (Lorente et al., 2015) based on the analysis of nonvelocity-based diagnostic parameters and the validation against in situ observations from a point-wise current meter (PCM) installed in B1 buoy (Fig. 1-a). The directional accuracy of HFR was rated at better than 8°, suggesting that the radar sites were properly calibrated. The correlation coefficient and RMSE values emerged in the ranges [0.58–0.83] and [4.02–18.31] cm s^{-1}, respectively, in accordance with prior results reported in the literature (Paduan et al., 2006; Kaplan et al., 2005; Emery et al., 2004). Moreover, the observed consistent concordance between HFR-derived synoptic surface current patterns and known aspects of the surface deltaic circulation from historical studies gives added confidence to HFR measurements as a solid benchmark for the rigorous skill assessment of IBI performance.

The present work builds upon Lorente et al. (2015) by integrating the HFR network with the CMEMS IBI regional predictive model to properly portray the ocean state and its variability. Observations from Ebro Delta HFR have been combined with IBI outputs since this synergistic approach can provide a comprehensive characterization of the highly dynamic coastal circulation and gain from the complementary nature of both systems. The main objective of this paper is fourfold. Firstly, to carry out an extensive observations-model (HFR-IBI) comparison aimed at determining the goodness of fit between the two technologies for deducing surface currents (Kuang et al., 2012). The exhaustive validation of OOFSs against independent measurements constitutes a core activity in oceanographic operational centers (Blockley et al., 2013; Lellouche et al., 2012) since it aids to: i) identify the relative strengths and weaknesses in the modeling of several key physical processes; ii) deepen the understanding of discrepancies in model predictions (Maraldi et al., 2013); iii) compare different versions of the same OOFS and evaluate potential improvements and degradations before a new version is transitioned into operational status (Martin, 2011). In

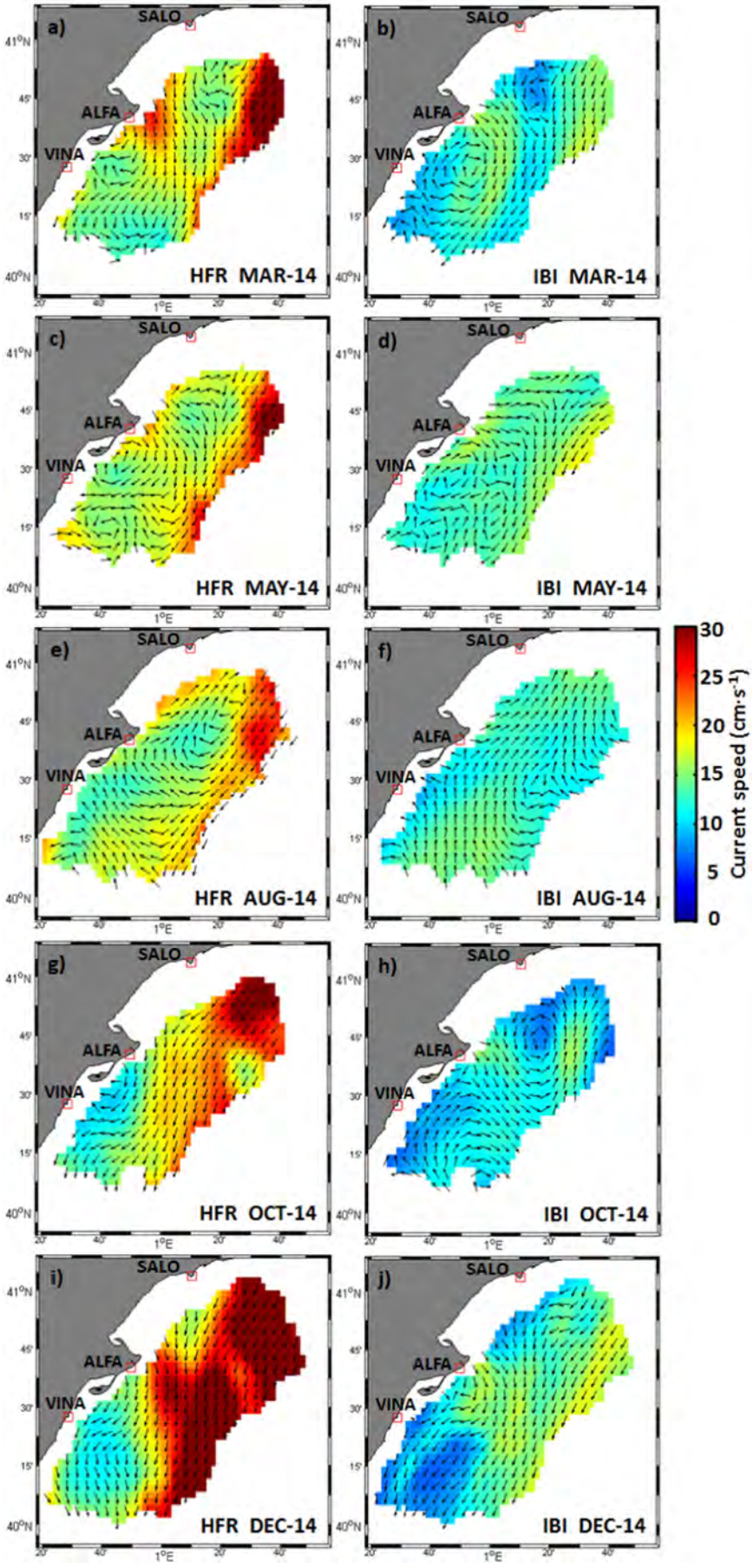
a)
SALO
ALFA
VINA
HFR MAR-14
b)
IBI MAR-14
c)
HFR MAY-14
d)
IBI MAY-14
e)
HFR AUG-14
f)
IBI AUG-14
g)
HFR OCT-14
h)
IBI OCT-14
i)
HFR DEC-14
j)
IBI DEC-14
41°N
40°N
1°E
30
25
20
15
10
5
0
Current speed (cm·s⁻¹)

this framework, an inter-institutional collaboration is in progress to establish common comparison schemes and skill metrics to deduce both the consistency and quality of OOFSs. In the present work, emphasis is placed on the consistency of monthly-averaged gridded outputs, defined as class-1 metrics (Hernandez et al., 2015; Hernandez et al., 2009).

Secondly, to verify IBI capabilities in reproducing the prevailing circulation features derived from HFR observations and previously reported in Lorente et al. (2015), namely: the predominant density-driven southwestward (SW) flow, the Ebro River impulsive-type freshwater discharge or the coastal clockwise eddy confined south of Ebro Delta mouth. In this context, surface eddies in the NW Mediterranean Sea have been earlier detected and tracked by HFR (Allou et al., 2010), satellite thermal images (Rubio et al., 2005) and models (Garreau et al., 2011) in order to understand the genesis of strong-lived vortices and their subsequent advection. The model skill assessment is completed with an analysis of monthly-averaged surface current maps and the exploration of dominant modes of variability in time and space through both an empirical orthogonal function (EOF) decomposition and a spectral analysis. Complementarily, eddy kinetic energy maps have been computed as indicators of intra-annual variability of the flow around the mean.

Thirdly, to investigate the relative contribution of local wind as one of the main forcing mechanisms typically associated with estuarine–ocean exchange and its importance as a predominant driving agent in Ebro Delta shelf (Carrillo et al., 2008; Maidana et al., 1999). The response of the subtidal surface current field to prevalent wind regimes in the area is examined in terms of induced circulation structures and immediacy of reaction by performing a conditional averaging approach and a time-lagged correlation analysis, respectively.

The ultimate goal is to evaluate the potential of CMEMS IBI as a consistent parent forecast system able to propagate the large-scale dynamics into a coastal fine-resolution OOFS through coherent open boundary conditions (Kourafalou et al., 2015). A downscaling approach is currently being implemented to operationally monitor the circulation in Port of Tarragona and the Ebro Delta area (Fig. 1-a) and capture small-scale coastal interactions which are not always properly represented in coarser resolution OOFSs. This initiative has been launched within the frame of SAMOA (Sistema de Apoyo Meteorológico y Oceanográfico de la Autoridad Portuaria) project, co-funded by Puertos del Estado (PdE) and 18 Spanish Port Authorities and aimed at putting in place an integrated suite of high-resolution meteorological and coastal hydrodynamic models in order to produce refined port-scale forecasts and increase the efficiency of marine operations in ports and harbours.

It is worth mentioning that this work is limited to the most surface layer. Therefore, a variety of factors that can influence the flow pattern have been excluded from the study. An investigation of stratification, topography and the impact of high freshwater inputs from the Ebro River deserves a detailed exploration which is beyond of the scope of the present paper.

This paper is organized as follows: Section 2 briefly overviews the main oceanographic features of the study area. Section 3 presents the specific instrumentation and briefly describes the configuration of IBI OOFS. Section 4 describes the observations-model comparison metrics, the data treatment and statistical methods used for the data analysis, followed in Section 5 by a detailed discussion of the results. Finally, main conclusions are summarized in Section 6.

2. Study area

The circulation in Ebro continental margin is mainly thermohaline and characterized by a quasi-permanent barotropic shelf-slope jet which flows southwestwards. This current, called Liguro-Provenzal-Catalan current or simply 'the North Current', is in geostrophic balance with the so-called Catalan front, which is a permanent density front associated to strong salinity gradients (Font et al., 1988a). Such density front, maintained by Ebro River runoff, separates two different surface water masses: light coastal and continental-influenced waters from saltier, and usually warmer, open sea waters (Salat et al., 2002).

The quasi-permanent SW flow is only altered by clockwise inertial oscillations (with maximum occurrence during the warm stratified season) and some short periods of current reversals, related to mesoscale events like frontal instabilities, meanders, eddies and filaments (Grifoll et al., 2015; Garreau et al., 2011; Birol et al., 2010; Font, 1990). The intensity of mean currents is relatively low (10–20 $cm \cdot s^{-1}$) and increases in autumn as a result of both the intensification of the mesoscale activity and the local wind variability (Font et al., 1995).

The Ebro Delta is a storm wave dominated coast, with a low-period mean wave climate (Palanques et al., 2002). The tidal influence in the continental shelf current field is very weak as expected for a microtidal and low-energy environment (Jimenez et al., 2002). The marine circulation near the delta, although dominated by the alongshore large-scale dynamics, presents a complex structure strongly influenced by the topography (widening of the shelf and the sharp change in the continental slope direction - Fig. 1-a) - and also by the seasonal variability of the remarkable Ebro River discharge rates, the changing wind conditions and the water column thermal stratification (Font et al., 1988b; Salat et al., 2002). The buoyancy input introduced by large freshwaters fluxes (particularly during the spring freshet), together with topographic effects, lead to the development of well-documented hydrographic features such as anticyclonic eddies on both sides of the delta and reinforce the shelf/slope front that drives the general circulation to the south (Carrillo et al., 2008; Salat et al., 2002; Font, 1990).

North of the delta, the flow originated near the river mouth tends to flow initially northwestward, but the confluence with the main current and the topographic influence of the lobate delta generate a clockwise eddy. This coherent vortex traps suspended materials and organic microcontaminants of industrial origin (coming from the nearing Tarragona industrial area, depicted in Fig. 1-a) that are subsequently sedimented southward (Font et al., 1987). Therefore, the Ebro river plume can play a first-order role in the transport and dispersal of anthropogenic contamination in the coastal zone.

The wind regime in the Ebro delta region can be classified into three groups: (i) northwesterly winds (also called 'mistral') are dominant during the cold season, from October to May (Font, 1990). They are both the strongest (with velocities up to 100 km/h) and the most persistent winds in the area; (ii) southwesterly winds ('garbins'), typical of the summertime and linked to fair weather conditions, are warm, weak and variable; (iii) onshore winds related to storms generated in the western Mediterranean basin. They mainly come from the NE ('gregal') and E ('llevants').

Although local winds are not directly responsible for the main characteristics of the marine circulation over the Ebro shelf (Font, 1990), surface current variability can be influenced by wind action if it is strong and steady enough (Espino et al., 1998). Local winds can develop significant inertial oscillations in spring (Font et al., 1988a) and contribute partially to the intensification of the currents during the cold season. Persistent and high-intensity NW wind jets channeled by the narrow Ebro valley introduce negative vorticity in the flow south of the Ebro Delta, reinforcing a local anticyclonic circulation on the shelf and producing northwestward currents near the coast (Espino et al., 1998; Han et al., 1983).

Fig. 2. Monthly averaged surface velocity fields, based on unfiltered hourly HFR (left) and IBI (right) current data, for (a–b) March, (c–d) May, (e–f) August, (g–h) October and (i–j) December 2014. The study area is not uniformly covered since only radar grid points satisfying a minimum data return of 50% over the monthly record have been considered. Only one grid point of every two is plotted for visualization reasons.

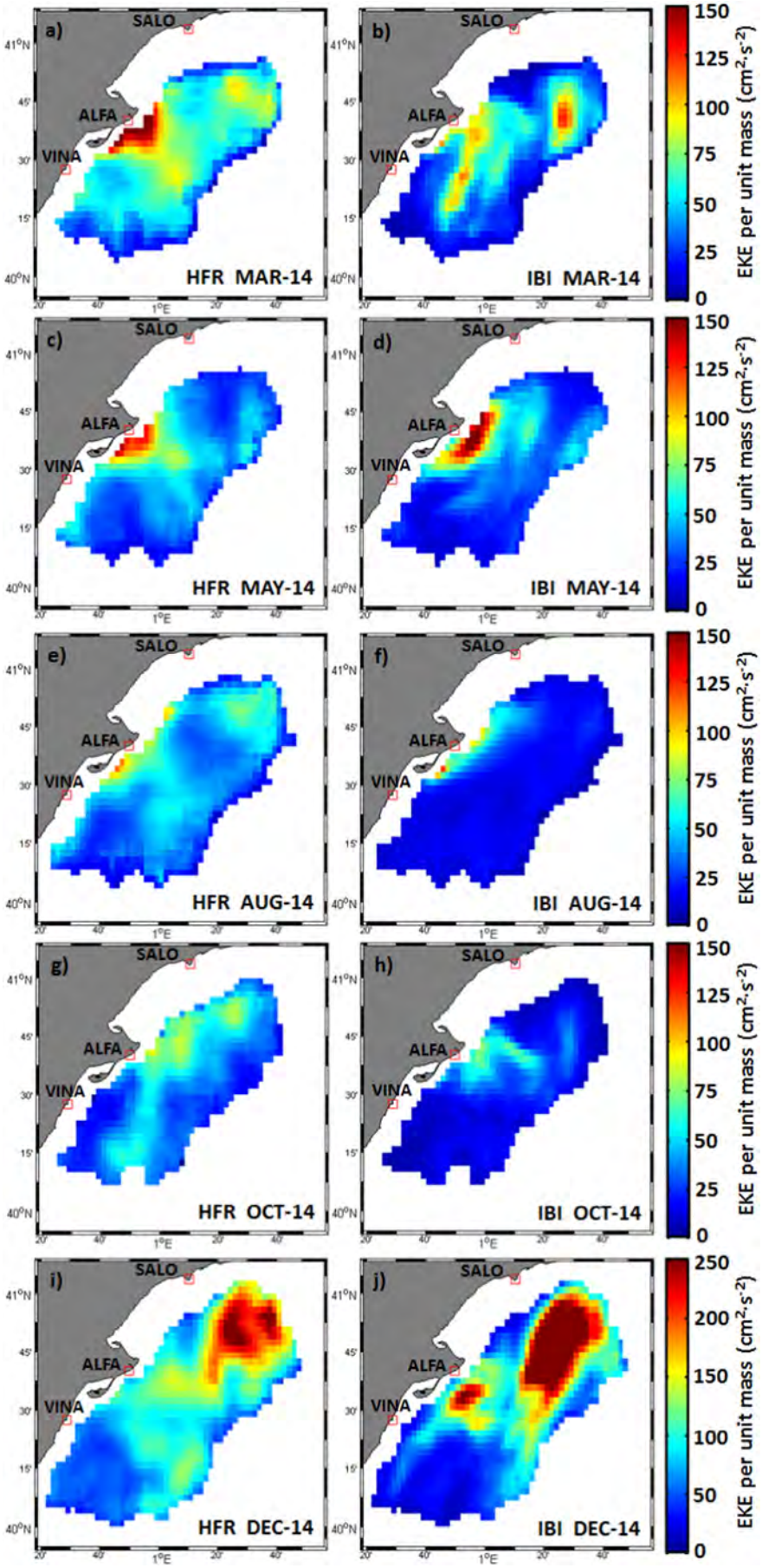
a)
SALO
ALFA
VINA
HFR MAR-14
b)
IBI MAR-14
c)
HFR MAY-14
d)
IBI MAY-14
e)
HFR AUG-14
f)
IBI AUG-14
g)
HFR OCT-14
h)
IBI OCT-14
i)
HFR DEC-14
j)
IBI DEC-14
41°N
45'
30'
15'
40°N
1°E
EKE per unit mass (cm²·s⁻²)
150
125
100
75
50
25
0
250
200

3. Instrumentation

3.1. HF radar (HFR)

A CODAR SeaSonde standard-range HFR system was deployed at Ebro Delta in December 2013 within the frame of RIADE (Redes de Indicadores Ambientales del Delta del Ebro) project. The system is owned by the Spanish Ministry of Agriculture and Environmental Affairs (www.magrama.gob.es) and currently operated by PdE for scientific purposes. The HFR network consists of an array of three remote shore-based sites (Fig. 1-a): Salou (SALO), Vinaroz (VINA) and Alfacada (ALFA), operating at a nominal frequency of 13.5 MHz with a 90 KHz bandwidth. Each site provides hourly radial measurements with a cut-off filter of 100 $cm \cdot s^{-1}$ and representative of current velocities in the upper first meter of the water column. Only calibrated (measured) antenna beam patterns were employed by the manufacturer supplied software to process radial data used in the present study, with the aim of maximizing HF radar usefulness for operational applications (Lipa et al., 2006; Kohut and Glenn, 2003). Ideal radial vectors (not calibrated, produced with the theoretical cosine antenna pattern) were already tested in Lorente et al. (2015) but the statistical results (not shown) revealed that they were not as accurate as calibrated radial data. In regions of overlapping coverage from two or more sites, radial current measurements are geometrically combined with the averaging radius set to 6 km in order to estimate hourly averaged total current vectors on a predefined Cartesian regular grid with 3 × 3 km horizontal resolution. The maximum horizontal range is set to 80 km and the angular resolution is 5°.

The hourly HFR data used in this study were collected during the entire 2014. The radar site overall performances were found to be consistent, with the three sites up and operational in excess of 95% of the time. Temporal data coverage was quantified by computing the percent of total possible vector returns at each radar grid point (Fig. 1-a). Percent coverage decreased rapidly near the outer edges of the domain where error levels were higher and quantified by larger Geometric Dilution of Precisions (GDOPs, Chapman and Graber, 1997), defined as unit-less multiplicative factors of the noise associated with the geometry of the HFR measurement. Only radar grid points satisfying a minimum data return of 50% over the 2014 annual record were considered in order to screen out the less reliable data (which usually presented GDOPs values above 1.5).

3.2. Buoy B1

The spatial coverage of Ebro Delta HFR includes an ocean Seawatch buoy deployed since August 2004: Tarragona buoy (40.68°N, 1.47°E, 688 m depth), hereafter referred to as B1 (Fig. 1-a). This instrument belongs to the Spanish deep water buoy network operated by PdE and is equipped with an acoustic PCM providing quality-controlled hourly averaged current velocity vectors at a nominal depth of three meters. According to the manufacturer (Falmouth Scientific Inc.), the instrumental error is around 0.5 $cm \cdot s^{-1}$. A wind speed and direction sensor manufactured by R. M. Young Company measures mean hourly wind data (computed from 5 min recording) at a height of three meters, used here as a proxy for the local open sea wind conditions. It should be noted that current and wind records were only available from 1 May to 31 October 2014. B1 suffered from brief communication outages during this period and subsequent short gaps (2 − 3 h) in data time series were linearly interpolated.

3.3. The IBI operational ocean forecasting system

A variety of OOFSs are currently running over the western Mediterranean basin, encompassing CMEMS core model solutions and other downscaling modeling techniques such as the SOCIB WMOP system (Juza et al., 2015b). Among the formers, IBI presents the highest horizontal grid resolution (1/36°) whereas the Mediterranean Sea and Mercator Global Ocean Physics Analysis and Forecast systems have a 1/16° and 1/12° model configuration, respectively (Tonani et al., 2009; Lellouche et al., 2012). Since small-scale coastal ocean processes are not always adequately reproduced by coarser resolution OOFSs, an increased mesh resolution is required to achieve the aforementioned objectives.

The IBI Monitoring and Forecasting Center (IBI-MFC) provides a real-time short-term 5-day hydrodynamic forecast (and one day of hindcast as best estimate) of currents and other oceanographic variables, such as temperature, salinity and sea level. IBI is based on an eddy-resolving Nucleus for European Modeling of the Ocean (NEMO) model application (v3.4) that includes high-frequency processes required to characterize regional-scale marine processes. As previously indicated, such application is run at 1/36° horizontal resolution (~2 km) on a Cartesian regular grid size of 1093 × 1894 points, with a domain extending between 19°W-5°E and 26°N-56°N (Fig. 1-b). The NEMO model (Madec, 2008) solves the three-dimensional primitive equations in spherical coordinates discretized on an Arakawa-C grid and 50 geopotential vertical levels (z coordinate), assuming hydrostatic equilibrium and Boussinesq approximation. Further details about the model configuration and the skill assessment can be found in Sotillo et al. (2015) and also in Aznar et al. (2016).

4. Methods

4.1. Observations-model comparison metrics

In order to accurately compare the IBI hindcast product and HFR data, the two grids must be matched. To this aim, radar estimations have been bilinearly interpolated on the more refined IBI regular grid (1/36°). Monthly averaged maps of Eulerian surface currents have been calculated for HFR and IBI to explore the prevalent circulation patterns during 2014. Eddy kinetic energy (EKE) maps, obtained from the unfiltered hourly current data, have been computed as indicators of the flow variance. The mean EKE per unit mass, defined as:

$$EKE = \sum_{i=1}^{N} \frac{\left[(u_i - u_m)^2 + (v_i - v_m)^2\right]}{2N} \quad (1)$$

has been determined for each and all of the grid points (Kovačević et al., 2004), where u_i and v_i represent eastward and northward hourly velocity components, N is the total number of observations and u_m and v_m are the corresponding monthly mean values for each particular grid node.

Spatial patterns of the complex correlation coefficient and its associated phase (Kundu, 1976), together with scalar correlation and RMSE between observed and modeled current components (zonal and meridional), have been also estimated on a monthly basis. All correlations cited were significant at the 95% confidence level (Emery and Thomson, 2001, p. 253), unless otherwise indicated. The main aim has been to investigate the temporal evolution of radar-model agreement for 2014 and to understand the potential sources of discrepancies.

Fig. 3. Monthly averaged maps of Eddy Kinetic Energy (EKE), based on unfiltered hourly HFR (left) and IBI (right) current data, for (a–b) March, (c–d) May, (e–f) August, (g–h), October and (i–j) December 2014.

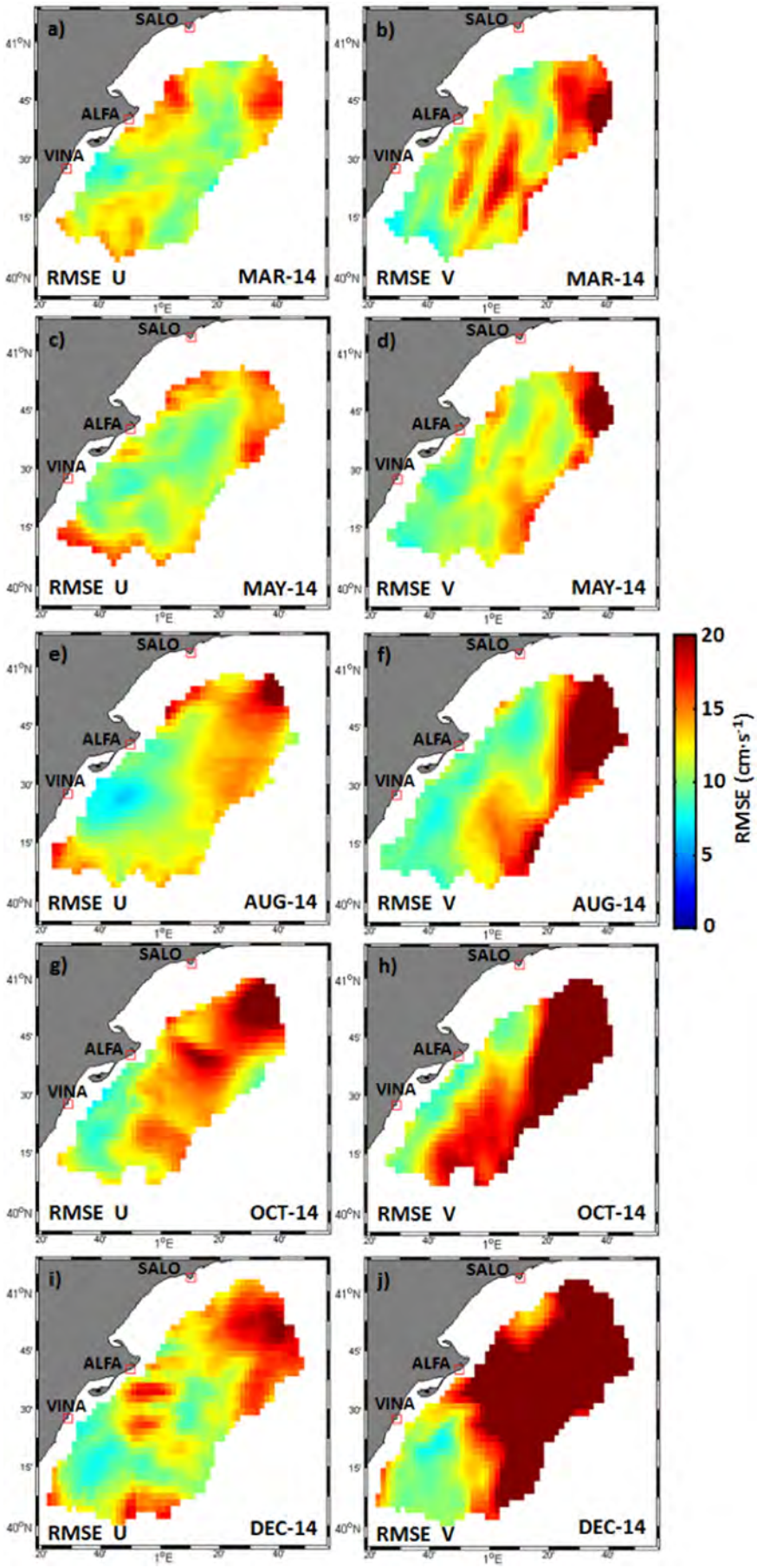
a)
SALO
ALFA
VINA
RMSE U
MAR-14
b)
RMSE V
MAR-14
c)
RMSE U
MAY-14
d)
RMSE V
MAY-14
e)
RMSE U
AUG-14
f)
RMSE V
AUG-14
g)
RMSE U
OCT-14
h)
RMSE V
OCT-14
i)
RMSE U
DEC-14
j)
RMSE V
DEC-14
41°N
40°N
1°E
20
15
10
5
0
RMSE (cm·s⁻¹)

4.2. Characterization of the spatiotemporal variability of surface circulation field

Rotatory spectral analyses (Gonella, 1972) have been performed for hourly current data from B1, modeled currents and HFR-derived total vectors at the grid point (P1) closest to B1 location. The examination has been conducted for a 6-month period May–October 2014 of concurrent records in order to identify the dominant modes of temporal variability. Complementarily, a second grid point (P2) has been chosen to evaluate spectral variations between near-shore and offshore regions. To ensure the continuity of the data record, small gaps detected (not larger than 3 h) in time series have been linearly interpolated. Spectra have been calculated by dividing time series into successive six day segments, with a 50% overlap and a Hanning window (Emery and Thomson, 2001), and subsequently averaged to provide some smoothing. Confidence levels for spectra densities have been derived assuming a chi-squared distribution for the variance.

Complementarily, a complex Empirical Orthogonal Function (EOF) decomposition has been used to explore the driving forces and spatiotemporal scales behind the variability of sea surface currents (Kundu and Allen, 1976). This method, which reduces the components of the vector field to a complex scalar, has become widespread in order to extract the dominant modes of variability. The representative spatial patterns (or EOF modes) and their corresponding temporal coefficients or principal components (PCs, which describe the evolution of the modes) are determined by using the singular value decomposition of the covariance matrix.

EOF analysis has been applied to HFR and IBI current velocity datasets using the raw (unfiltered) hourly time series for the entire year 2014. Main spatial modes obtained have been interpreted in terms of physical processes related to the detected spatially coherent structures. Since EOFs are purely statistical, each EOF mode's significance has been evaluated according to the rule of thumb proposed by North et al. (1982), where only those modes containing a significant portion of the total variance are considered to properly reproduce the observed surface current fields. Finally, the standardized PCs associated with each radar-model EOF mode have been quantitatively compared by means of linear correlation coefficients in order to assess the level of agreement.

4.3. Wind-induced circulation

The hourly wind vector dataset registered at B1 buoy during May–October 2014 has been low-pass filtered (cut off period of 30 h), depicted and later analyzed at quarterly time-scale by means of rose plots to deduce the prevailing wind directions over the study area. In addition, wind measurements have been decomposed into principal components to infer the main axis of variability. The associated conditionally-averaged subtidal current patterns under these dominant conditions have been subsequently extracted with the aim of illustrating the wind-driven low frequency response. This methodology, based on the division of specific wind events according to prevalent directions (within 45° around the variance axis orientation) and speed above a certain threshold (3 m/s), has been previously adopted in several of studies (Mihanović et al., 2011; Gačić et al., 2009). Finally, the mean circulation fields obtained for HFR and IBI have been qualitatively examined for four different wind regimes related to the major and minor axis of wind variability.

Complementarily, the flow response has been investigated by comparing the PCs associated with IBI and HFR with the PCs of local wind (Lana et al., 2016). The correlation coefficient has been also calculated for the winds in all directions to determine the angle for which the relationship is maximized. Finally, the association between wind and flow variability has been studied for wind data and sub-surface currents measured at B1 and surface velocity estimations provided by HFR and IBI at the nearest grid point. To this purpose, a time-lagged complex correlation analysis has been used to explore the current response for a 24-hour interval.

5. Results and discussion

5.1. IBI skill assessment and dominant features of the surface flow

The sequence of monthly averaged current maps reveals the moderate resemblance between HFR data and IBI modeled currents in terms of main circulation features in the study-area, in spite of some distinguishing peculiarities (Fig. 2). The main discrepancy lies in the evident underestimation of the intensity of the southwestward flow (the North Current), which is properly captured in terms of predominant direction during the months of March, August and December (Fig. 2-b, d, j. respectively). For August, the North Current is absent from the modeled current pattern and probably displaced to the east, according to the tiny clockwise eddy and the onset of the current reversal observed in the eastern edge of the study domain (Fig. 2-f). In the case of October, IBI clearly fails to capture basic details of the coastal circulation (Fig. 2-h).

During March, the SW shelf-slope jet and the Ebro River impulsive-type freshwater outflow are clearly evidenced (Fig. 2-a, b), although higher velocities are detected for HFR. The monthly-averaged freshwater discharge measured at Tortosa hydrological station (Fig. 1-a) during this month was around 600 $m^3 \cdot s^{-1}$, reaching a peak of 1300 $m^3 \cdot s^{-1}$ during the first days.

Equally, the confinement of a coastal anticyclonic eddy in the south of Ebro Delta can also be observed in radar and modeled data. In the case of the latter, the vortex structure is more developed in March. However, it presents a similar position, diameter and elongation direction during May (Fig. 2, c-d). The lifetime of this hydrodynamic feature is rather alike, formed during January and absent of the monthly picture from August to December. The steady weakening of both the SW slope flow and the signal of the Ebro river plume are shown in both datasets.

During August (Fig. 2, e–f), a noticeable current reversal in coastal areas is observable, presumably due to a well-documented change in the predominant local wind regime during this stage of the year (Garreau et al., 2011; Font, 1990). The inversion of the inshore flow is scarcely influenced by the Ebro River freshwater discharge as it reaches one of its lowest values during the summertime (150 $m^3 \cdot s^{-1}$). Indeed, in the case of IBI the reversal is more expanded along the shelf and the aforementioned SW jet is missing from the picture, with a tiny clockwise eddy enclosed in a general poleward flow (Fig. 2, f). By contrast, a pronounced anticyclonic recirculation cell is shown by HFR, detached from the shore (Fig. 2, e). Such detachment is in accordance with previous modeling exercises in the NW Mediterranean where a burst of southeasterlies and northerlies, after a long period of mistral winds, appeared to disengage coastal eddies (Garreau et al., 2011).

The main observations-model differences arise in October (Fig. 2, g-h): HFR exhibits a fairly homogeneous and intensified SW along-shore flow, whereas IBI presents a more intricate circulation pattern characterized by two eddies with different vorticity. Moreover, it is noteworthy the coastal counter current directed northeastward and the inversion of the SW slope jet. By the end of 2014, the monthly spatial patterns become rather uniform, revealing the acceleration of the SW flow (especially for HFR) until reaching ultimately a peak strength in December (Fig. 2, i–j). The intense Ebro River outflow is also observable (as the monthly-averaged value is around 600 $m^3 \cdot s^{-1}$), together with the presence of small-scale coastal meanders.

With regards to the variability of the flow, monthly-averaged maps of EKE exhibit similar spatial distribution along 2014, with higher values

Fig. 4. Monthly averaged maps of zonal (left) and meridional (right) root mean squared error (RMSE) between HFR and IBI surface current data for (a–b) March, (c–d) May, (e–f) August, (g–h), October and (i–j) December 2014.

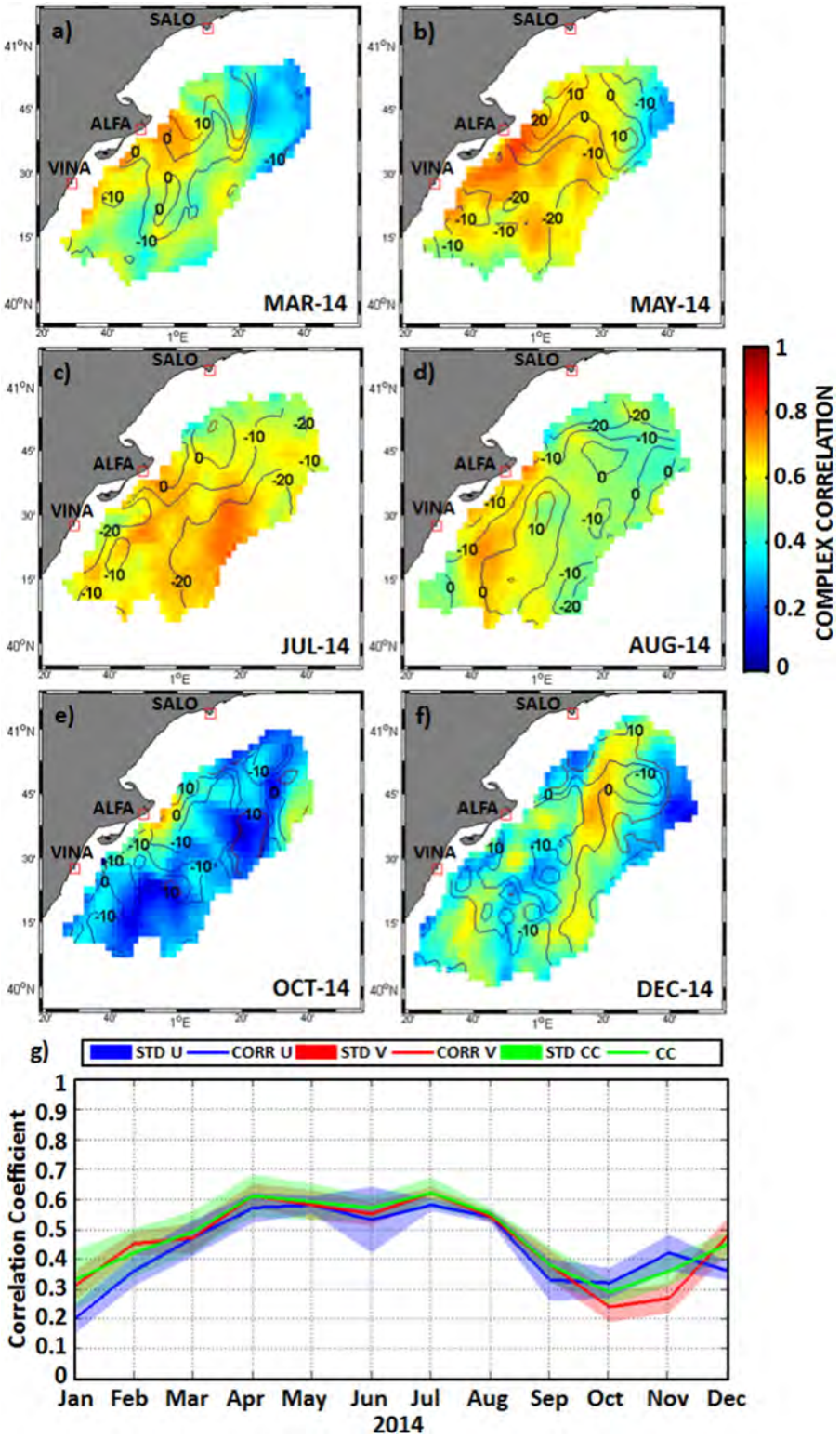

Fig. 5. Monthly averaged maps of complex correlation between HFR and IBI surface current data for (a) March, (b) May, (c) July, (d) August, (e) October and (f) December 2014. Isolines represent the phase (in degrees): positive (negative) values denote counter-clockwise (clockwise) rotation of IBI vectors respect HFR vectors. (g) Monthly evolution of spatially averaged skill metrics (scalar correlation - CORR U and CORR V - and complex correlation - CC - coefficients). Shaded values reveal the standard deviation associated with each metric.

tending to be allocated in areas where the mean circulation is strongest (Fig. 3). In March, a non-uniform dipole-like structure is detected in both datasets (Fig. 3, a–b), although IBI presents one core more stretched in the along-shore direction. Peaks of EKE are located in the Ebro River mouth (NE part of the domain) in the case of observed (modeled) currents. In May, similar maximum values of EKE are concentrated on areas adjacent to Ebro deltaic region, despite HFR (IBI) shows a predominant cross-shore (along-shore) configuration (Fig. 3, c–d). During August, the peak of flow variance reaches the lowest value along the coastline due to the weakening of the SW flow and the barely noticeable Ebro River freshwater discharge rates (Fig. 3, e–f). By October, a slight increase of EKE is observed in both radar and

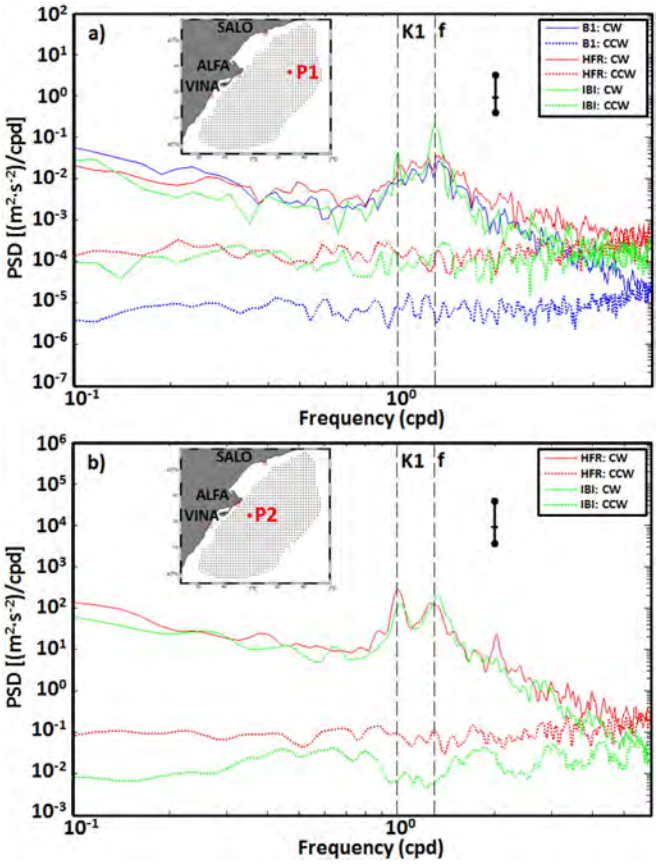

Fig. 6. (a) Power spectral density of the rotary auto-spectra of B1 buoy (blue) and HFR (red) and IBI (green) at the grid point P1 (the closest to B1 location), performed for a 6-month period May–October 2014 of concurrent records. Clockwise (counter-clockwise) components are represented by solid (dotted) lines. (b) Power spectral density of the rotary auto-spectra of HFR (red) and IBI (green) at the near-shore grid point P2. Vertical dashed lines indicate the frequencies of the diurnal constituent (K_1) and the inertial oscillations (f). Error bars indicate the 95% confidence interval. (For interpretation of the references to colour in this figure legend, the reader is referred to the web version of this article.)

IBI datasets (Fig. 3, g–h), presumably due to the reported increase of the mesoscale activity in autumn (Font et al., 1995). Finally, a relevant peak of EKE is detected in the northeast area of the study domain (stronger for modeled currents) as a result of the aforementioned acceleration of the SW slope jet (Fig. 3, i–j). A secondary maximum can be observed close to ALFA radar station, although in the case of IBI is stronger and clearly detached from the main peak.

The analysis of skill metrics reveals higher RMSE values for the meridional velocity component, with the main radar-model disagreement generally detected at the outer edges of the study domain (Fig. 4). Particularly noticeable is that the lowest errors (4–9 $cm \cdot s^{-1}$) can be found in the proximity of the shoreline during the summer (Fig. 4, e–f), with values increasing up to 15–17 $cm \cdot s^{-1}$ during the spring as a result of an increase of the freshwater discharge, not fully captured by the modeled solution (Fig. 4, a–d). This could be attributable to the fact that IBI includes as runoff forcing in the Ebro River Delta the simulations from SMHI E-HYPE hydrological model instead of real-time in situ observations. Significant differences in current speed (RMSE above 20 $cm \cdot s^{-1}$) are observed during the last part of 2014 (Fig. 4, g–j), when an acceleration of the SW along-shelf flow is evidenced (Fig. 2, g–j).

The observed radar-model discrepancies are in the range 7–26 $cm \cdot s^{-1}$, with spatially-averaged RMSE values around 13 and 16 $cm \cdot s^{-1}$ for the zonal and meridional velocity components, respectively. Albeit relevant, they are in accordance with some RMSE values previously reported in the literature, ranging from 10 to 28 $cm \cdot s^{-1}$ (O'Donncha et al., 2015), from 8.8 to 21.5 $cm \cdot s^{-1}$ (Ren et al., 2015) or from 5 to 30 $cm \cdot s^{-1}$ (Yu et al., 2012). Furthermore, O'Donncha et al. (2015) found that mean RMSE across Galway bay equalled 23.8 $cm \cdot s^{-1}$ for December 2011. By contrast, lower scalar RMSE values (8–14 $cm \cdot s^{-1}$) have been also stated in other prior works (Cosoli et al., 2013).

Monthly-averaged maps of complex correlation (CC) reflect an overall higher HFR-IBI agreement in areas close to the shoreline, with the correlation coefficients and the associated veering angles close to 0.8 and 0°, respectively, during the first part of 2014 (Fig. 5, a–d). Both parameters usually lie in the ranges of [0.3, 0.8] and [−10°, 10°], respectively, although lower values of the CC coefficient can be found for October and December (Fig. 5, e–f). The observations-model concordance generally decreases at the outer edges of the domain, especially toward the NE where higher uncertainty levels (i.e., higher GDOP values) are found in radar estimations (Lorente et al., 2015; Lorente et al., 2016). The CC coefficient drops to [0.3–0.5] and the related (absolute) phase can reach 20° in areas near the borders of the spatial coverage (Fig. 5, d). The monthly evolution of spatially-averaged metrics (Fig. 5, g) demonstrates a mean CC coefficient around 0.5 for March (Fig. 5, a) and a closer HFR-IBI match during April–August as illustrated by CC values reaching 0.6 (Fig. 5, b–d). By the onset of autumn, a decrease in model skill is observable since correlation coefficients fluctuate around 0.3 for October (Fig. 5-e, g), followed by a later recovery in IBI accuracy during the last part of 2014 with CC values above 0.6 in several areas of the domain for the specific case of December (Fig. 5-f, g).

The CC coefficient and the associated veering angle are in line with the available literature on radar-model comparisons. In particular, Cosoli et al. (2013) and O'Donncha et al. (2015) reported coefficients in the range 0.2–0.6 and 0.3–0.8, respectively, with the related phase spanning between° 0 and 20° (absolute value). In terms of spatially-averaged CC coefficients, Yu et al. (2012) shown a CC coefficient comprised between 0.1 and 0.6, similar to the results depicted in Fig. 5-g. According to the results, IBI OOFS is able to capture the observed broad-scale features and statistically reproduce monthly patterns in terms of mean and variance despite some model drawbacks detected in relation to the reduced energy content in surface current speeds. Assuming there are inherent constraints that restrict the observations-model approach (i.e., sensor limitations, instrumental noise, differences in depth sampling, small-scale energetic processes unresolved by the model, etc.), IBI has proven to be a rather consistent OOFS in the study-area. Some model limitations could be due to the large-scale offshore circulation in the entire Mediterranean basin not included in the present numerical configuration. In addition, the determination of the skill level necessary for a given application is context specific. Existing discrepancies between IBI (regional-scale OOFS) and coastal–scale dynamics and the spatio-temporal distribution of model errors should be interpreted according to a variety of factors like the difficulty in accurately simulating both the Ebro River outflow or the inadequate spatio-temporal resolution of the meteorological forecasts used as forcing mechanism in a complex coastal region where topographical steering further impacts on flows (O'Donncha et al., 2015).

5.2. Characterization of the spatiotemporal variability of the surface circulation

Spectral analyses have been computed for a 6-month period May–October 2014 (warm stratified season) when B1 buoy was operative in order to examine power spectral discrepancies in the frequency domain between PCM measurements and HFR data and IBI outputs in the grid point P1 (the closest to B1 location, Fig. 6-a). The three of them present qualitatively similar characteristics, capturing properly the dominant features within the diurnal and inertial bands, related to significantly prevalent clockwise (CW) rotatory motions (solid lines). Relevant polarized peaks are evident for the three datasets, although the amplitudes are significantly larger for IBI currents (solid green

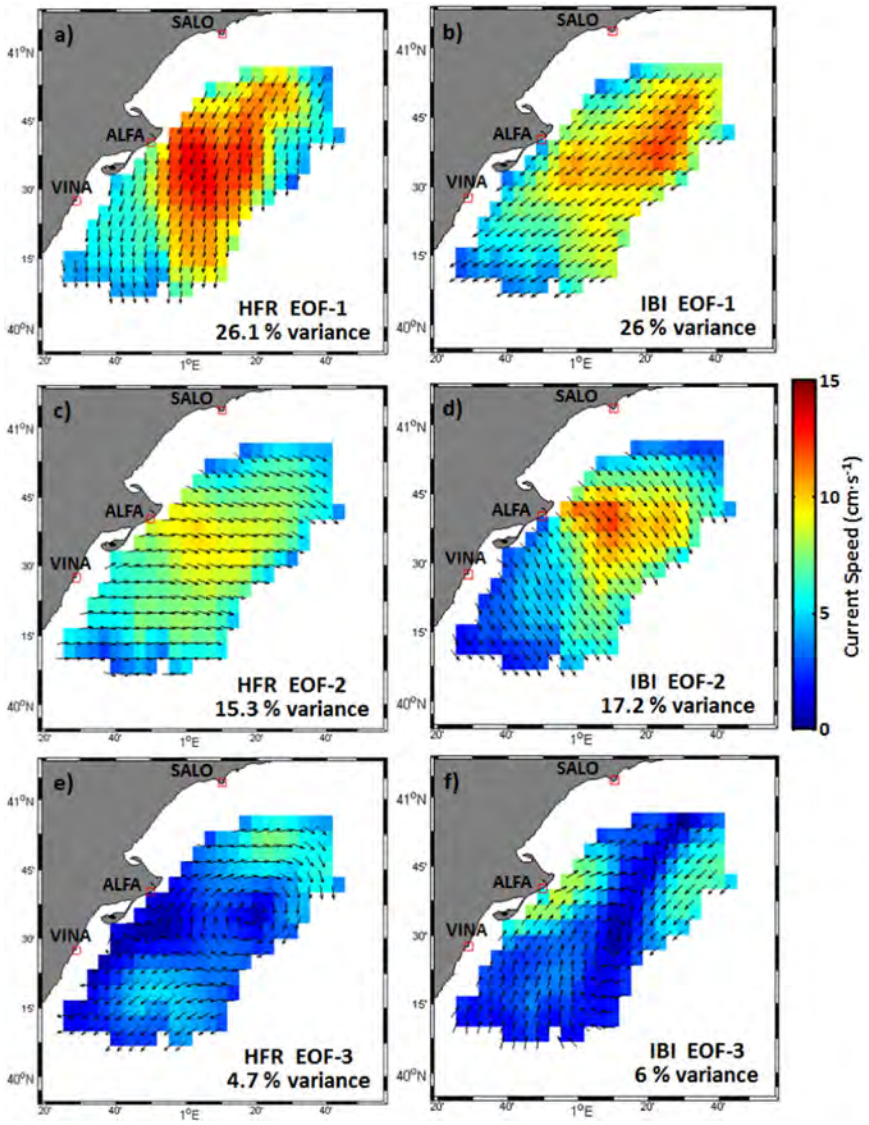

Fig. 7. Spatial patterns of the (a–b) first, (c–d) second and (e–f) third EOF dominant modes derived from unfiltered hourly HFR (left) and IBI (right) surface currents for 2014. Current vectors were plotted in every second grid point for clarity. Variance explained is indicated in the lower right corner of the corresponding panel.

line). The inertial peak is the most pronounced, pointing out the adjustment of the stratified fluid to the wind driven currents and, subsequently, the importance of local wind as forcing mechanism. Indeed, such amplitude difference in the inertial peak could be attributable to an overestimation of the modeled wind speed (addressed in Section 5.4). Offshore oscillations in this frequency band are a common feature in ocean circulation and their presence in the NW Mediterranean has been previously documented (Schaeffer et al., 2011a; Font, 1990).

Spectral variations between near-shore and offshore regions have been investigated for a second grid point (P2) using HFR and IBI estimations (Fig. 6, b). Once more, the prevalence of the positive rotational motion over the rectilinear ones is evidenced, along with a strong radar-model resemblance. Both datasets exhibit well-resolved peaks with similar amplitudes at inertial and diurnal frequencies, highlighting the importance of the land-sea breeze in coastal circulation. It is also noteworthy that surface currents at P2 present higher energy levels than in P1 (Fig. 6-a), in accordance with the maximum values of EKE which are generally concentrated in the vicinity of Ebro River mouth (Fig. 3). Finally, a drop of energy and later flattening about 10 cpd are common for the CW components of the three types of spectra.

By contrast, the counter-clockwise component (CCW, dotted lines) is much less energetic in both P1 and P2 grid points (especially in the case of B1 current estimations) and is where the main differences in variance distribution between B1 and both HFR and IBI can be found. In P2, the model underestimation of the CCW component could be explained in terms of an inadequate representation of the vertical density stratification, which plays a relevant role by modulating the wind-induced circulation and also the development of eddy structures.

5.3. Empirical orthogonal function (EOF) analysis

The EOF analysis (Fig. 7), performed on the unfiltered data set containing relevant high-frequency spatiotemporal variability, confirmed that the surface current field evolved in space and time according to three dominant modes of variability, which accounted for the 46.1% (49.2%) of the total variance in the case of HFR (IBI). According to the rule of thumb applied (North et al., 1982), higher modes were not statistically significant.

A year-round overall prevailing SW shelf-slope jet is described by the first mode (Fig. 7, a–b). The spatially homogeneous pattern, rather similar to the annual averaged current map (not shown), basically captures the North Current pathway. EOF-1 represents the

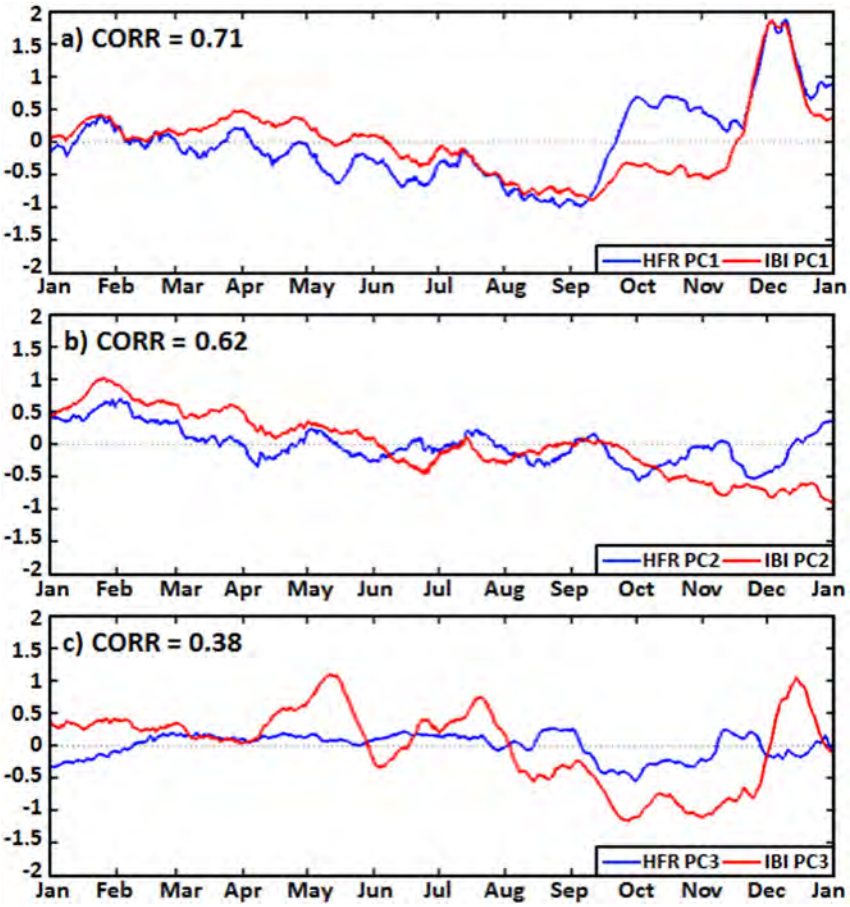

Fig. 8. Time coefficients (PC) of the (a) first, (b) second and (c) and third EOF mode of hourly HFR (blue) and IBI (red) current data set evaluated for the entire year 2014. Time series have been filtered with a 20 day running mean. The corresponding linear correlation coefficient is provided in the upper left corner of each panel. (For interpretation of the references to colour in this figure legend, the reader is referred to the web version of this article.)

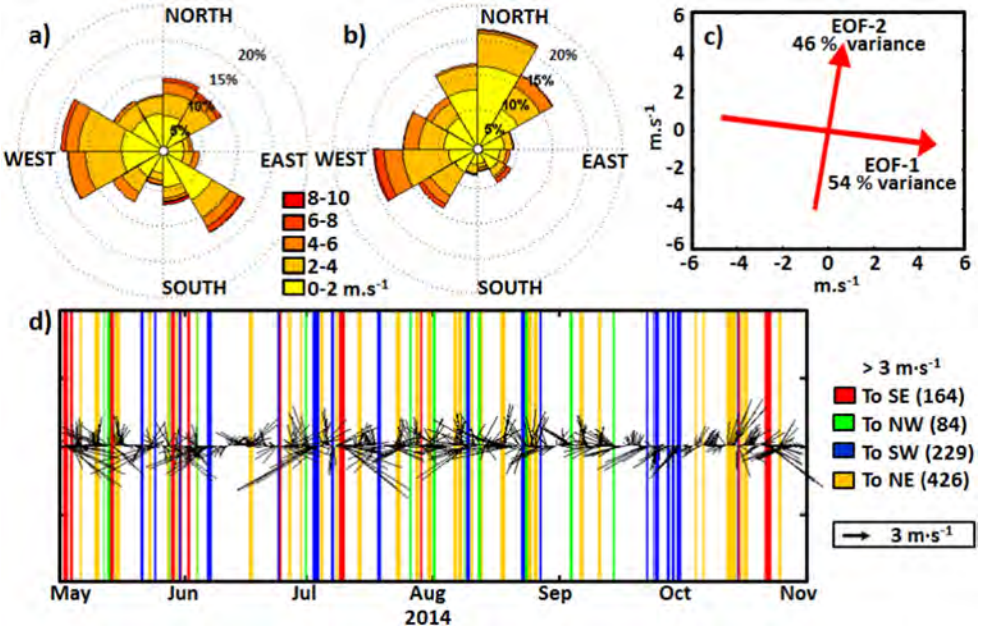

Fig. 9. Low-passed (cut-off period of 30 h) wind rose plots for (a) May–June–July (MJJ) and (b) August–September–October (ASO), showing the predominant propagation directions. (c) Main axes of variability for hourly wind data registered at B1 buoy. (d) Stick diagram of low-passed hourly-averaged wind vectors for the 6-month study period, with a classification of intense (>3 $m \cdot s^{-1}$) wind events according to the main axes of variability.

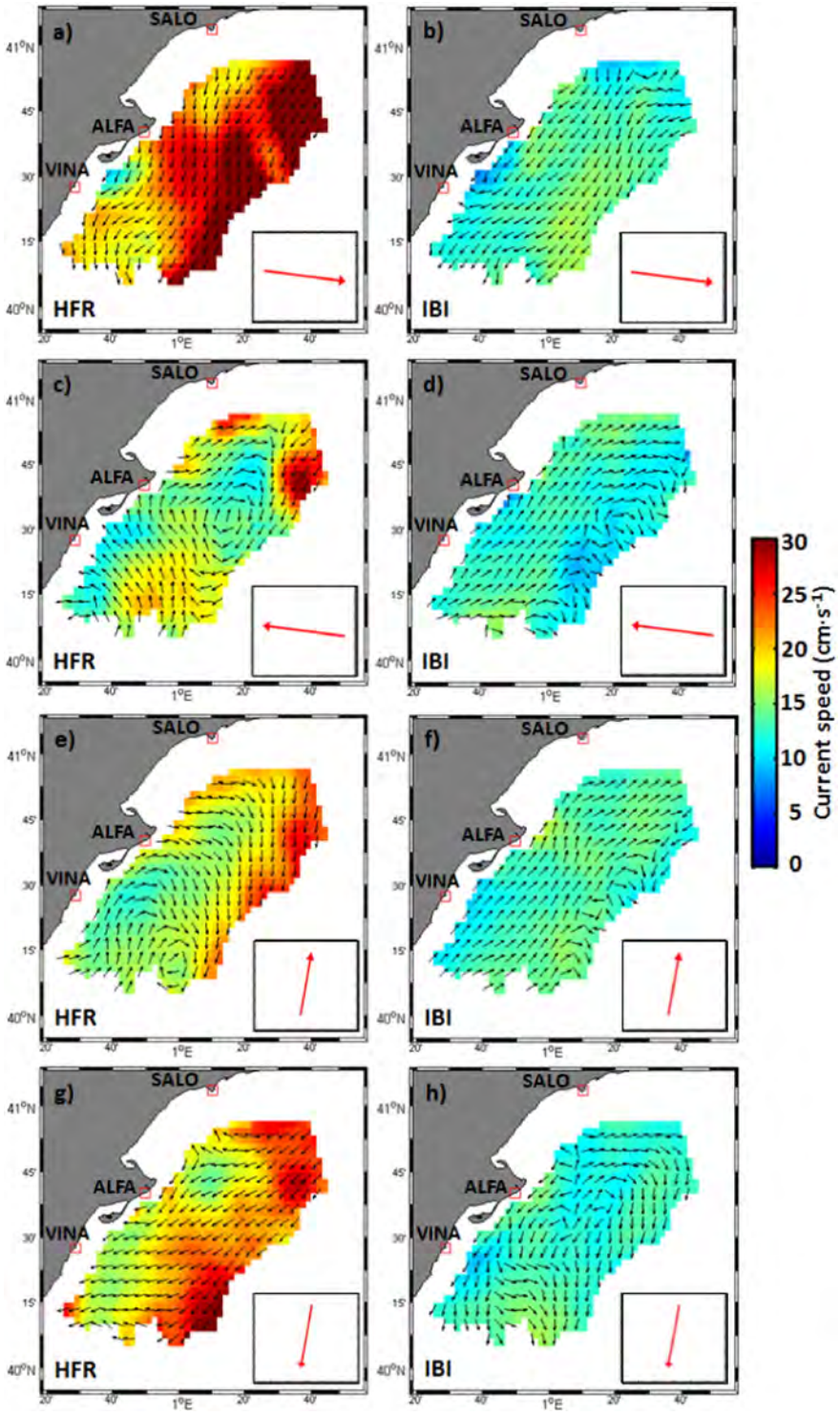

Fig. 10. Conditionally-averaged subtidal current patterns derived for HFR (left) and IBI (right) hourly surface data, according to the main axis of wind variability (direction denoted in the lower right corner).

21.6% and 26% of the total variance for HFR and IBI, respectively. The other two HFR (IBI) modes are superimposed onto EOF-1, accounting for the 15.3% (17.2%) and 4.7% (6%) of the variance, respectively. The second mode captures the cross-shelf circulation (Fig. 7, c–d), with a well-defined offshore-directed flow perpendicular to EOF-1. The third mode adds some heterogeneity to the basic uniform patterns represented by the first two modes, since it introduces curvature to the current field (Fig. 7, e–f).

At first glance, EOF-1 (EOF-2) spatial patterns derived from HFR and IBI outputs are similar in terms of intensity and direction of current vectors. Some differences arise in the southern half of the study area where HFR vectors present a more pronounced meridional (zonal) tendency to the south (east). The main discrepancies are detected in EOF-3: although both systems introduce complexity by adding vorticity in the form of a large (albeit weak) anticyclonic recirculation cell, they do it in distinct ways. In the case of HFR, a clear divergence of the main

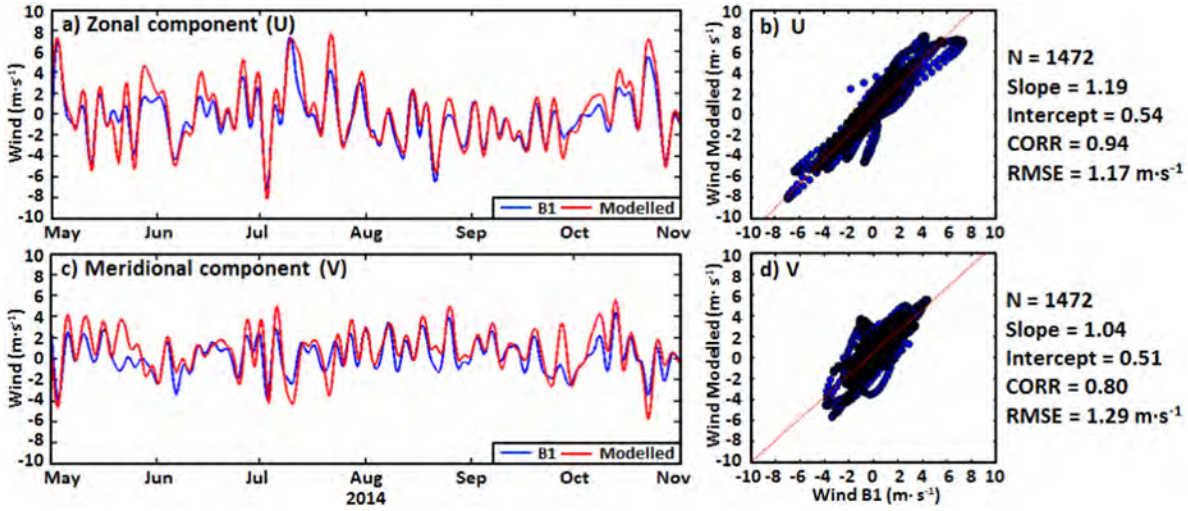

Fig. 11. Comparison of low-pass filtered (cutoff period of 30 h) time series of wind measured at B1 buoy (blue line) and modeled (red line) at the grid point closest to B1 location for the zonal (a) and meridional (c) components. The corresponding best linear fit of scatter plots and the metrics derived are presented for the zonal (b) and meridional (d) components. (For interpretation of the references to colour in this figure legend, the reader is referred to the web version of this article.)

flow is observed in the southernmost part of the spatial domain (Fig. 7, e), whereas IBI reveals a fully-developed CW eddy, with the associated core slightly displaced to the south-west part of the domain (Fig. 7, f).

The temporal variation in the strength of these three EOF modes is represented by their corresponding time coefficients or principal components (PCs), shown in Fig. 8. In the case of HFR, PC1 is predominantly positive except during the May–September period (Fig. 8-a, blue line), becoming again strongly positive during the autumn and reaching a peak by December, in clear agreement with the strengthened shelf-slope SW jet shown in Fig. 2-i. The first principal component of IBI (red line) is in close agreement with HFR-PC1 (as highlighted by a linear correlation coefficient of 0.71) and satisfactorily reproduces the intensification of the SW flow by December. However, noticeable disparities can be observed in October and the first fortnight of November when HFR (IBI) is positive (negative), explaining thus the sharp decrease in IBI performance previously detected for this month (Fig. 5-e, g). The negative values of PC1 during summer are in concordance with periods of current reversals during the stratified warm season earlier reported (Grifoll et al., 2015; Birol et al., 2010; Font, 1990).

The temporal structure of HFR-PC2 (Fig. 8-b, blue line) reveals a principal offshore-directed flow through January–March period and also in late December, which are months characterized by both predominant mistral winds and high freshwater discharge rates. Although IBI-PC2 (red line) is similar and significantly correlated (above 0.6) to HFR-PC2, the discrepancies found during the last quarter of 2014 can justify the lower than expected HFR-IBI agreement during this period (Fig. 5-g). This is especially true for December when a relevant concordance of both PC1 has been evidenced.

Table 1
Statistics of comparison between local wind registered at B1 buoy and modeled wind at the grid point closest to B1 location, for a 6-month period of concurrent records. Time series have been low-pass filtered (cut-off period of 30 h). Complex correlation (CC) coefficient and veering angle are shown. Positive angles indicate model winds to the right of the observed winds. RMS differences between observed and modeled wind speed are also depicted.

Period (2014)	N	CC coefficient	CC veering (°)	RMSE (m/s)
May–October	1472	0.92	12.38	1.27
May	248	0.86	11.99	1.75
June	240	0.96	20.02	0.91
July	248	0.94	15.02	1.62
August	248	0.94	9.84	0.64
September	240	0.83	5.77	0.88
October	248	0.96	12.24	1.38

Lastly, HFR-PC3 (Fig. 8-c, blue line) adds clockwise curvature during most part of the year (February–September and November), whereas IBI-PC3 (red line) generally exhibits higher absolute values. The level of agreement between both PC3 is lower than those obtained for the two first principal components, with the correlation coefficient below 0.4 and the main differences (in terms of opposite sign) detected for January, August and December.

An overall acceptable observations-model match can be inferred from the cumulative and partial percentages of variance retained by the first three dominant EOFs, which are in accordance with prior percentages reported in the literature (Cosoli et al., 2013; Kaplan et al., 2009). The surface flow patterns derived from the first two EOF modes and their corresponding principal components present a good resemblance, with the main disagreement arising from the temporal evolution of PC3.

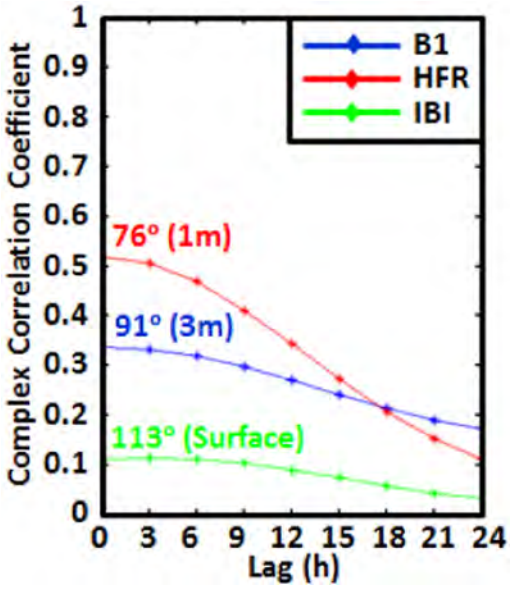

Fig. 12. Time-lagged vector correlation analysis between local wind registered at B1 buoy and the sub-surface currents measured by B1 (blue), HFR (red) and IBI model (green) current data at the grid point closest to B1 location. The mean veering angle at zero-lag and the corresponding depth of current estimations are also indicated. (For interpretation of the references to colour in this figure legend, the reader is referred to the web version of this article.)

Table 2
Correlation coefficients between the principal components (PCs) of the first two EOF modes of wind (registered at B1) and the first two EOF modes of HFR and IBI. The amplitudes have been filtered with a 1 day running mean.

Currents	Principal components	WIND (B1)	
		PC1	PC2
HFR	PC1	0.52	−0.28
	PC2	0.47	0.67
IBI	PC1	0.39	−0.43
	PC2	−0.02	−0.14

5.4. Forcing mechanisms

Low-pass filtered time series of wind measurements registered at B1 have been depicted on a quarterly basis with the aim of defining the prevalent wind directions (Fig. 9, a–b). According to the wind roses, there was an evident change in the local wind regime from spring-early summer (MJJ, Fig. 9-a) to late summer-autumn (ASO, Fig. 9-b). During the former period, the wind was primarily from the second (S-E) and fourth (N-W) quadrants. During the latter, the predominant wind directions were by contrast from the first (N-E) and third (S-W) quadrants, with a remarkable reduction of northwesterly wind events (the most energetic ones).

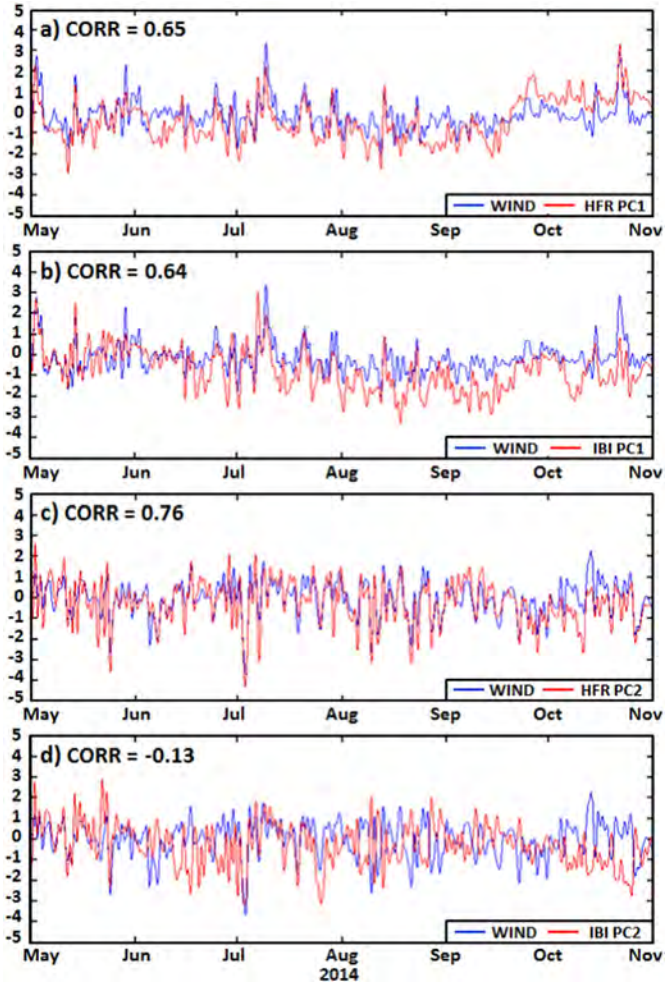

Fig. 13. Comparison of the first principal component (PC1, red line) of HFR (a) and IBI (b) with the local wind (blue line) projected onto the propagation direction for which the wind-current relationship is maximized: 145° clockwise from the North. Comparison of the second principal component (PC2, red line) of HFR (c) and IBI (d) with the local wind (blue line) projected onto the propagation direction of maximum correlation: 41° clockwise from the North. The amplitudes have been normalized by their respective standard deviations and filtered with a 1 day running mean. (For interpretation of the references to colour in this figure legend, the reader is referred to the web version of this article.)

Complementarily, the major and minor variance axes have been determined (Fig. 9-c), revealing that the main variability occurs along a direction 99° azimuth containing the 54% of the total energy. This is the EOF1 mode, presumably aligned with persistent and intense northwesterly mistral winds channeled by the narrow Ebro Valley as reported by Grifoll et al. (2015) and Font (1990), among others. The orthogonal EOF2 mode is oriented 9° clockwise from north and holds the remaining 46% of the variance, capturing mainly the influence of alongshore winds. Although a predominance of EOF1 (EOF2) during MJJ (ASO) can be readily deduced, it is incorrect to assume that mistral winds do not occur in the second quarter. Wind data registered at B1 have been categorized into the four different dominant regimes when the speed exceeded a threshold of 3 $m \cdot s^{-1}$ and the associated events computed with the aim of characterizing the typical current patterns (Fig. 9-d). There was a predominance of alongshore wind events (655), whereas cross-shore wind episodes (248) represented the 27% of the cases during the 6-month study period analyzed.

For northwesterly wind episodes, the average circulation maps provided by HFR and IBI look alike in terms of direction but clearly differ in the current speed due to a relevant model underestimation (Fig. 10, a–b). Intense mistral winds appear to transfer the energy to the uppermost layer by accelerating and organizing the surface flow to the southwest, consistent with Ekman transport to the right of the wind direction. Once again, modeled currents reveal a significantly reduced energy content in spite of capturing the small-scale coastal meander (SW of the study area) and the reinforcement of both the shelf-slope jet and onshore currents in the vicinity of Ebro River mouth.

As response to southeasterlies, the wind-induced circulation to the NW becomes noticeable in HFR-derived map (Fig. 10, c). The interaction of the cross-shelf flow on the southern inner shelf with topographic obstacles gives rise to a shift to the right of the coastal flow. The current reversal joins the riverine discharges to subsequently close a clockwise vortex structure by converging with the predominant SW flow. By contrast, no evidence of such anticyclonic gyre can be observed in the modeled pattern (Fig. 10, d), which seems to be more homogeneous near the shoreline and noisier at the eastern border of the domain. The coastal currents flowing northeastwards eventually shift to the right in order to (presumably) join the quasi-permanent shelf-slope jet to SW, which is absent of the picture and probably displaced to the east.

In the case of southwesterly wind episodes, only shallow coastal waters appear to be driven to the NE until merging with the stronger Ebro River outflow to the east (Fig. 10, e). As a consequence of the convergence of this combined flow with the prevalent SW jet, a small, detached clockwise eddy is generated in the southernmost region. On the contrary, modeled currents are clearly weaker and fully aligned to the NE (Fig. 10, f), presenting a strong resemblance with the conditionally-averaged map shown in Fig. 10-d.

The HF radar-derived circulation map reveals a reinforcement of the SW slope jet when northeasterly winds are predominant, with the inner-shelf flow slightly deflected clockwise according to a classical Ekman drift and subsequently following the coastline to the south (Fig. 10, g). However, the modeled pattern presents a rather chaotic configuration over the core of the study domain (Fig. 10, h). Only coastal shallow currents appear to be driven by the wind and the SW slope jet does not seem to be accelerated by wind action.

Since IBI seems to moderately capture the overall circulation features associated with wind EOF-1 but not to reproduce the observed current patterns related to wind EOF-2, potential observations-model discrepancies have been interpreted in terms of the differences arising from the 6-month comparison between the observed hourly local wind (corrected from 3 m recorded height to 10 m standard height)

and the modeled 10-m three-hourly wind field at the grid point closest to B1 (2.5 km away), used as forcing mechanism in IBI OOFS (Fig. 11). A similar methodology was previously applied by Muscarella et al. (2011) in order to assess the accuracy of forecasted winds in Delaware Bay. The comparison of low-passed (cutoff period of 30 h) modeled time series with the local wind registered at B1 reveals a significantly high agreement for the zonal component, with a correlation coefficient (CORR) of 0.94 (Fig. 11, a–b). However, the level of concordance for the meridional component is lower (Fig. 11, c–d), as reflected by the smaller (higher) CORR (RMSE) value of 0.80 (1.29 $m.s^{-1}$). This could presumably explain the observations-model disagreement found when local winds predominantly blow alongshore (Fig. 10, e–h) as the meridional component plays a major role for this type of wind regime. In addition, an overestimation of the local wind is evidenced, according to the slopes (>1) and intercept (>0.5) values obtained from the best-linear fit of both velocity components (Fig. 11- b, d).

Regarding the monthly complex correlation magnitude between observed and modeled wind, the coefficient is above 0.92 during the 6-month study period (except in May and September, when it drops to 0.86 and 0.83, respectively) and the associated veering angle is noticeable, with values ranging from 5° to 20° (Table 1). Positive angles indicate model winds to the right of the observed winds. Such deflection explains the predominantly negative veering (between −10° and −20°) previously detected in some areas of the study domain when comparing modeled and observed surface currents, indicating a clockwise rotation of IBI vectors respect HFR vectors (Fig. 5, b–e). Likewise, the monthly RMSE between the wind speeds are also relevant, lying in the range [0.64, 1.75] $m \cdot s^{-1}$.

The meteorological forecast used as forcing mechanism in IBI OOFS has not been employed to analyze the wind-induced circulation over the entire domain due to the existence of both a wind speed overestimation and also a phase mismatch between the modeled and observed inertial signal. In this context, a more skillful atmospheric forecast model with a higher spatiotemporal resolution (i.e., hourly prediction over a more refined grid) could aid to better represent the coastal circulation in the Ebro Delta. Previous works in the NW Mediterranean have demonstrated the importance of wind model's high spatial resolution to discriminate topographic structures and better replicate inertial oscillations and mesoscale activity, whereas the temporal resolution plays a relevant but secondary role (Cerralbo et al., 2015; Schaeffer et al., 2011a).

Complementarily, the time-lagged vector correlation analysis shows the prompt current response to wind forcing (Fig. 12). The correlation peak is observed between 0-hour and 3-hour time lag, and is followed by the decay in correlation amplitude, steeper in the case of HFR. A similar approach was adopted in Ebro inner shelf by Grifoll et al. (2015), obtaining a significant correlation peak (0.33) at zero lag between cross-shelf water transport and cross-shelf wind registered by a buoy. In our case, an Ekman-like response to the right of the wind forcing is evidenced by the mean veering angle: 76° (91°) for HFR (B1) measurements representative of current velocities in the upper first meter (at a nominal depth of three meters) of the water column. The increase of deflection angles with depth also reveals the development of the Ekman spiral motion.

In the case of modeled currents, they appear to be poorly correlated with local wind when all types of wind events are considered, as highlighted by a correlation coefficient of 0.12. This modeling issue has been previously documented near other Deltas as the strong freshwater-induced haline stratification of the water confines most of the wind momentum input to the surface layer, while the subsurface current is mostly influenced by the open sea circulation (Bajo et al., 2014). Since this poor-relationship could be also partially attributable to an inexact representation of vertical density stratification during the warm season by IBI OOFS, further research should be undertaken to shed light on it. Previous works in the NW Mediterranean have probed that the surface signature of inertial motions in the uppermost part of the ocean can be easily captured by HFR in the presence of strong stratification which is confined to the mixed layer (Shrira and Forget, 2015). In this context, the complex correlation of local wind with HFR current measurements could be used as a proxy of the strength of the stratification, as previously demonstrated by Kohut et al. (2004) and Warrick et al. (2007).

Linear correlation coefficients have been computed between the principal components (PCs) related to the two main EOF modes of variability of local wind at B1 and the first two PCs associated with both modeled and radar-derived currents (Table 2). The influence of local wind forcing on HFR PC1 mode has been assessed, with a correlation coefficient of 0.52 (−0.28) for wind PC1 (PC2). This finding highlights the impact of energetic northwesterly mistral winds on the predominant SW flow, by inducing a classical Ekman drift at the sea surface with currents deflected clockwise with respect to the wind forcing. This wind-current interaction in Ebro Delta is in accordance with earlier works reported in the literature. Espino et al. (1998) demonstrated such relationship when winds are strong and steady enough. Grifoll et al. (2015) stated that the prevalent southwestward along-shelf flow was induced by the three-dimensional regional response to cross-shelf winds and the coastal constraint. Similarly, the PC1 of modeled currents seems to support previous statements as the correlation coefficients are 0.39 and −0.43 for PC1 and PC2 of wind, respectively (Table 2). The negative correlation coefficients obtained for the wind-current relationship in the along-shore direction reveal that northeasterly wind events play a relevant role by accelerating the prevalent SW flow, which is even more evident for IBI currents (−0.43) that for HFR velocities (−0.28).

The high correlation between the principal components can be readily seen in Table 2, with a value of 0.47 (0.67) for wind-PC1 (PC2) and HFR-PC2, respectively. The relevant accordance of PC2 between wind and HFR appears to be consistent with Ekman transport to the right of the wind direction. On the other hand, northwesterly mistral wind events (PC1) are expected to enforce the prevalent offshore-directed circulation regime represented by HFR EOF2 (Fig. 7-c) by increasing the mean speed of the flow. These results are again in good agreement with Grifoll et al. (2015), who demonstrated the interaction of wind with cross-shelf transport in shallow waters of Ebro Delta shelf. By contrast, the second principal component related to IBI appears to be barely correlated with the wind (Table 2), especially when along-shore winds (PC2) are predominant.

Complementarily, the flow response is examined by comparing the principal components of HFR and IBI with the wind projected onto each propagation direction in order to infer the angle for which the correlation coefficient reaches a peak (Fig. 13). In the case of PC1 (i.e., SW current flow), the maximum correlation is found with winds toward 145° clockwise from the North (i.e., northwesterly mistral winds): 0.65 and 0.64 for HFR and IBI, respectively (Fig. 13, a–b). In the case of PC2 (i.e., offshore-directed circulation regime), the wind-HFR relationship is maximized when local wind blows toward 41° from the North, with the correlation coefficient rated at 0.76 (Fig. 13-c). These results confirm the existence of an Ekman-like response of sub-surface currents by shifting to the right of local wind. However, the principal component related to IBI-EOF2 appears to be barely correlated, not only with southwesterly wind events (Fig. 13-d) but with any kind, in agreement with results gathered in Table 2.

6. Concluding remarks and future work

In this paper, particular emphasis has been devoted to the integration of a monitoring HFR network and the CMEMS IBI regional predictive model, working in tandem to properly portray the ocean state and its variability. This observations-model synergistic approach has demonstrated to be valid to describe the complex coastal circulation in the Ebro Delta shelf despite the observed model drawbacks in terms of reduced energy content in surface currents (especially the meridional velocity component) and some inaccuracies in the wind-driven

low frequency response. Although IBI reproduces reasonably well some basic features of the monthly circulation patterns in terms of main direction and variance, the model clearly underestimates the intensity of the southwestward 'North Current'.

The EOF analysis has confirmed that the modeled surface current field evolved both in space and time according to three significantly dominant modes of variability which accounted for the 49.2% of the total variance, in close agreement with the results obtained for HFR (46.1%). A relevant observations-model resemblance has been evidenced for the three EOF spatial patterns, with similar partial percentages of variance retained by each mode. The detected decrease in IBI performance during the last quarter of 2014 (especially in October) has been explained in terms of the discrepancies arising from the PCs related to the first two EOF modes, although their annual correlation was remarkably high (0.71 and 0.62 for PC1 and PC2, respectively).

Although the first two HFR EOF modes have been found to be significantly influenced by local wind, only the IBI PC1 appeared to be correlated with the wind forcing. The wind-current interaction was maximized when the former blew toward SE (NE) in the case of PC1 (PC2) – i.e., when the main flow moves SW (SE), suggesting the existence of an Ekman-like response of the surface circulation.

Since IBI seemed not to properly reproduce the observed circulation patterns related to along-shore winds, observations-model discrepancies have been in part attributed to the existence of both a speed overestimation and also a phase mismatch between the modeled and observed winds. This also leads to an inertial peak of higher amplitude for the clock-wise component of IBI in the frequency domain, as shown in Fig. 6. Some of the limitations detected in IBI performance have been also hypothesized to be partially related to the inadequate spatiotemporal resolution of the wind field used as forcing mechanism of the surface circulation. This issue has been recently addressed during the pre-operational implementation of the SAMOA fine-scale coastal forecasting system, which is nested to IBI and forced with a higher resolution atmospheric model (hourly values over a 1/20° horizontal grid), based on HIRLAM (Cats and Wolters, 1996) and provided by the Spanish Meteorological Agency. Likewise, some IBI system shortcomings could be also attributable to the large-scale offshore circulation in the entire Mediterranean basin not included in the present numerical configuration. Notwithstanding, IBI has proved to be an acceptable large-scale regional "father" system, capable to resolve moderately well the background mesoscale shelf circulation in the Ebro Delta and thus be able to provide coherent open boundary conditions to nested fine-resolution coastal models.

A number of primary mechanisms driving coastal dynamics should be thoroughly investigated in the short-term future since they could exert significant influence on detected discrepancies. For instance the land-sea interaction, governed by the intense Ebro River runoff and the resulting buoyancy-driven circulation, must be evaluated together with the variability of the freshwater plume extension. The role of the underlying topography on the surface current variability is also noteworthy in steeper regions, acting as physical constraint of diverse coastal processes (Kohut et al., 2004). Therefore, a detailed bathymetry with the coastal geometry appropriately scaled is crucial for both IBI and nested OOFSs. Furthermore, an adequate representation of the density stratification is essential as it acts as a factor modulating not only the surface current response to wind-forcing but also the development of eddy structures. In this context, vorticity patterns are expected to have important consequences in terms of dispersion or retention of biogeochemical materials at local scales (Schaeffer et al., 2011b).

With the advent of new technologies (coastal altimetry, gliders, argo-floats, etc.), a combined use of multi-platform, multi-scale observing systems encompassing both in situ (buoys, tide gauges, etc.) and remote (HFR, satellite, etc.) sensors will provide further insight into the comprehensive characterization of the shelf's surface circulation. Equally, it will also contribute positively to a more exhaustive model accuracy assessment.

Noticeable efforts are in progress in order to define meaningful skill scores to quantitatively assess the quality and consistency of nested system outputs by setting up specific intercomparison exercises on the overlapping areas at diverse timescales (Bell et al., 2015). In particular, a future methodology to judge the strengths and weaknesses of OOFSs and evaluate their ability to out-perform larger scale systems could encompass the intercomparison of global configurations (the Mercator Global system), regional applications (CMEMS IBI) and higher resolution models at litoral/coastal scales (SAMOA), dynamically embedded in IBI OOFS.

Finally, the proposed observations-model strategy could be optimized by blending radar data and simulations to get the best surface current estimates (Stanev et al., 2015) and also by assimilating radar radial vectors (Marmain et al., 2014; Breivik and Saetra, 2001) on high-resolution coastal models implemented within the frame of SAMOA project. In this sense, data assimilation provides the integrative framework for maximizing the joint utility of HFR-derived observations and coastal circulation models. This approach could enhance predictive skills and facilitate high-stakes decision-making for coastal management and mitigation of environmental risks in the Ebro Delta area.

Acknowledgment

The authors gratefully acknowledge Qualitas Remos Company (partner of CODAR Ocean Sensors) for their useful suggestions.

References

Allou, A., Forget, P., Devenon, J.L., 2010. Submesoscale vortex structures at the entrance of the Gulf of lions in the northwestern Mediterranean Sea. Cont. Shelf Res. 30, 724–732.

Aznar, R., Sotillo, M.G., Cailleau, S., Lorente, P., Levier, B., Amo-Baladrón, A., Reffray, G., Álvarez-Fanjul, E., 2016. Strengths and weaknesses of the Copernicus forecasted and reanalyzed solutions for the Iberia-Biscay-Ireland (IBI) waters. J. Mar. Syst. 159, 1–14.

Bajo, M., Ferrarin, C., Dinu, I., Umgiesser, G., Stanica, A., 2014. The water circulation near the Danube Delta and the Romanian coast modelled with finite elements. Cont. Shelf Res. 78, 62–74.

Bell, M.J., Schiller, A., Le Traon, P.Y., Smith, N.R., Dombrowsky, E., Wilmer-Becker, K., 2015. An introduction to GODAE OceanView. Journal of Operational Oceanography 8, 2–11.

Bellomo, L., Griffa, A., Cosoli, S., Falco, P., Gerin, R., Iermano, I., Kalampokis, A., Kokkini, Z., Lana, A., Magaldi, M. G., Mamoutos, I., Mantovani, C., Marmain, J., Potiris, E., Sayol, J. M., Barbin, Y., Berta, M., Borghini, M., Bussani, A., Corgnati, L., Dagneaux, Q., Gaggelli, J., Guterman, P., Mazzoldi, A. Molcard, A. Orfila, A., Poulain, P.-M., Quentin, C., Tintoré, J., Uttieri, M., Vetrano, A., Zambianchi, E., Zervakis, V. (2015) Toward an integrated HF radar network in the Mediterranean Sea to improve search and rescue and oil spill response: the TOSCA project experience. Journal of Operational Oceanography, Vol. 8, Issue 2, pp. 95–107 http://dx.doi.org/10.1080/1755876X.2015.1087184.

Birol, F., Cancet, M., Estournel, C., 2010. Aspects of the seasonal variability of the Northern Current (NW Mediterranean Sea) observed by altimetry. J. Mar. Syst. 81, 297–311.

Blockley, E.W., Martin, M.J., McLaren, A.J., Ryan, A.G., Waters, J., Lea, D.J., Mirouze, I., Peterson, K.A., Sellar, A., Storkey, D., 2013. Recent development of the Met Office operational ocean forecasting system: an overview and assessment of the new Global FOAM forecasts. Geoscientific Model Dev Discuss 6, 6219–6278.

Breivik, Ø., Saetra, Ø., 2001. Real time assimilation of HF radar currents into a coastal ocean model. J. Mar. Syst. 28 (3–4), 161–182.

Carrillo, J.A., Redondo, J.M., Fraunie, P., Durand, N., 2008. Induced structures under seasonal flow conditions in the Ebro delta shelf. Laboratory and numerical models, Il Nuovo Cimento 31 (5–6), 771–790.

Cats, G., Wolters, L., 1996. The Hirlam project. Int. J. Comput. Sci. Eng. 3, 4–7.

Cerralbo, P., Grifoll, M., Moré, J., Bravo, M., Sairouní Afif, A., Espino, M., 2015. Wind variability in a coastal area (Alfacs Bay, Ebro River delta). Adv. Sci. Res. 12, 11–21.

Chapman, R.D., Graber, H.C., 1997. Validation of HF radar measurements. Oceanography 10 (2), 76–79.

Chavanne, C., Janeković, I., Flament, P., Pulain, P.-M., Kizmić, M., Gurgel, K.W., 2007. Tidal currents in the northwestern Adriatic: high-frequency radio observations and numerical model predictions. Journal of Geophysical Research 112, C03S21.

Cianelli, D., Falco, P., Iermano, I., Mozzillo, P., Uttieri, M., Buonocore, B., Zambardino, G., Zambianchi, E., 2015. Inshore/offshore water exchange in the Gulf of Naples. J. Mar. Syst. 145, 37–52.

Cosoli, S., Licer, M., Vodopivec, M., Malacic, V., 2013. Surface circulation in the Gulf of Trieste (northern Adriatic Sea) from radar, model, and ADCP comparisons. J. Geophys. Res. 118 (11), 6183–6200.

Coulliette, C., Lekien, F., Paduan, J.D., Haller, G., Marsden, J.E., 2007. Optimal pollution mitigation in Monterey Bay based on coastal radar data and nonlinear dynamics. Environ. Sci. Technol. 41 (18), 6562–6572.

Emery, W.J., Thomson, R.E., 2001. Data Analysis Methods in Physical Oceanography. Elsevier Science, Amsterdam.

Emery, B., Washburn, M.L., Harlan, J.A., 2004. Evaluating radial current measurements from CODAR high frequency radars with moored current meters. J. Atmos. Ocean. Technol. 21, 1259–1271.

Espino, M., Sanchez-Arcilla, A., Garcia, M.A., 1998. Wind induced mesoscale circulation off the Ebro Delta, NW Mediterranean: a numerical study. Journal of Marine Systems 16, 235–251.

Font, J., 1990. A comparison of seasonal winds with currents on the continental slope of the Catalan sea (Northwestern Mediterranean). J. Geophys. Res. 95 (C2), 1537–1545.

Font, J., Julia, A., Rovira, J., Salat, J., Danchez-Pardo, J., 1987. Circulación marina en la plataforma continental del Ebro determinada a partir de la distribución de masas de agua y los microcontaminantes orgánicos en el sedimento. Acta Geologica Hispanica 21-22, 483–489.

Font, J., Salat, J., and Tintore, J.: Permanent features of the circulation in the Catalan Sea. Pelagic Mediterranean Oceanography. Oceanologica Acta 9 (vol. sp.), pp. 51–57, 1988a.

Font, J., Salat, J., Wang, D.P., 1988b. Lagrangian and Eulerian observation of inertial oscillations in the shelf break offshore the Ebro River Delta (Catalan Sea, NW Mediterranean). Rapp. Comm. Int. Mer Médit 31, 201.

Font, J., Garcia-Ladona, E., Gorriz, E.G., 1995. The seasonality of mesoscale motion in the Northern Current of the Western Mediterranean: several years of evidence. Oceanologica Acta 18 (N2), 207–219.

Gačić, M., Kovačević, V., Cosoli, S., Mazzoldi, A., Paduan, J.D., Mancero-Mosquera, I., Yari, S., 2009. Surface current patterns in front of the Venice Lagoon. Estuarine, Coastal and Shelf Science 82 (3), 485–494.

Garreau, P., Garnier, V., Schaeffer, A., 2011. Eddy resolving modeling if the Gulf of Lions and Catalan Sea. Ocean Dyn. 61, 991–1003.

Gonella, J., 1972. A rotary-component method for analyzing meteorological and oceanographic vector time series. Deep Sea Research, Part II 19, 833–846.

Gopalakrishnan, G., Blumberg, A.F., 2012. Assimilation of HF radar-derived surface currents on tidal-timescales. Journal of Operational Oceanography 5 (1), 75–87.

Grifoll, M., Aretxabaleta, A.L., Espino, M., 2015. Shelf response to intense offshore wind. Journal of Geophysical Research, Oceans 120. http://dx.doi.org/10.1002/2015JC010850.

Guihou, K., Marmain, J., Ourmieres, Y., Molcard, A., Zakardjian, B., Forget, P., 2013. A case study of the mesoscale dynamics in the North-Western Mediterranean Sea: a combined data-model approach. Ocean Dyn. 63 (7), 793–808.

Han, G., Ballester, A., Kohler, K., 1983. Circulation on the Spanish Mediterranean continental shelf near the Río Ebro. In: Castellví, J. (Ed.), Estudio Oceanográfico de La Plataforma Continental. Buppr, Barcelona, pp. 137–148.

Hernandez, F., Bertino, L., Brassington, G., Chassignet, E., Cummings, J., Davidson, F., Drévillon, M., Garric, G., Kamachi, M., Lellouche, J.M., Mahdon, R., Matthew, J.M., Ratsimandresey, A., Regnier, C., 2009. Validation and intercomparison studies within GODAE. Oceanography 22 (3), 128–143.

Hernandez, F., Blockley, E., Brassington, G.B., Davidson, F., Divakaran, P., Drévillon, M., Ishizaki, S., Sotillo, M.G., Hogan, P.J., Lagemaa, P., Levier, B., Martin, M., Mehra, A., Mooers, C., Ferry, N., Ryan, A., Regnier, C., Sellar, A., Smith, G.C., Sofianos, S., Spindler, T., Volpe, G., Wilkin, J., Zaron, E.D., Zhang, A., 2015. Recent progress in performance evaluations and near real-time assessment of operational ocean products. Journal of Operational Oceanography 8 (S2), 221–238.

Iermano, I., Moore, A.M., Zambianchi, E., 2016. Impacts of a 4-dimensional variational data assimilation in a coastal model of southern Tyrrhenian Sea. J. Mar. Syst. 154, 157–171.

Jimenez, J.A., Guillen, J., Sanchez-Arcilla, A., Gracia, V., Palanques, A., 2002. Influence of benthic boundary layer dynamics on wind-induced currents in the Ebro Delta inner shelf. Journal of Geophysical Research 107 (C6), 3054 pp. 1–10.

Juza, M., Mourre, B., Lellouche, J.M., Tonani, M., Tintoré, J., 2015a. From basin to sub-basin scale assessment and intercomparison of numerical simulations in the Western Mediterranean Sea. J. Mar. Syst. 149, 36–49.

Juza, M., Mourre, B., Renault, L., Gómara, S., Sebastián, K., Lora, S., Beltran, J.P., Frontera, B., Garau, B., Troupin, C., Torner, M., Heslop, E., Casas, B., Vizoso, G., Tintoré, J., 2015b. Operational SOCIB forecasting system and multi-platform validation in the western Mediterranean Sea. Journal of Operational Oceanography http://dx.doi.org/10.1080/1755876X.2015.1117764 (in press).

Kaplan, D.M., Largier, J., Botsford, L.W., 2005. HF radar observations of surface circulation off Bodega Bay (northern California, USA). J. Geophys. Res. 110 (C10020), 1–25.

Kaplan, D.M., Halle, C., Paduan, J., Largier, J., 2009. Surface currents during anomalous upwelling seasons off central California. J. Geophys. Res. 114, C12026. http://dx.doi.org/10.1029/2009JC005382.

Kohut, J.T., Glenn, S.M., 2003. Improving HF radar surface current measurements with measured antenna beam patterns. J. Atmos. Ocean. Technol. 20, 1303–1316.

Kohut, J.T., Glenn, S.M., R.J., C., 2004. Seasonal current variability on the New Jersey inner shelf. Journal of Geophysical Research 109, C07S07. http://dx.doi.org/10.1029/2003JC001963.

Kourafalou, V.H., De Mey, P., Staneva, J., Ayoub, N., Barth, A., Chao, Y., Cirano, M., Fiechter, J., Herzfeld, M., Kurapov, A., Moore, A.M., Oddo, P., Pullen, J., Van Der Westhuysen, A., Weisberg, R., 2015. Coastal Ocean Forecasting: science drivers and user benefits. Journal of Operational Oceanography 8 (Supplement 1), 147–167. http://dx.doi.org/10.1080/1755876X.2015.1022348 (Special Issue: GODAE Oceanview part 1).

Kovačević, V., Gačić, M., Mancero, M.I., Mazzoldi, A., Marinetti, S., 2004. HF radar observations in the northern Adriatic: surface current field in front of the Venetian Lagoon. Journal of Marine Systems 51 (1–4), 95–122.

Kuang, L., Blumberg, A.F., Georgas, N.: Assessing the Fidelity of surface currents from a coastal ocean model and HF radar using drifting buoys in the middle Atlantic bight. Ocean Dyn., Vol. 62, Issue 8, pp. 1229–1243, 2012.

Kundu, P., 1976. Ekman veering observed near the ocean bottom. Jounal of Physical Oceanography 6, 238–242.

Kundu, P.K., Allen, J.S., 1976. Some three-dimensional characteristics of low-frequency current fluctuations near the Oregon coast. J. Phys. Oceanogr. 6, 181–199.

Lana, A., Marmain, J., Fernández, V., Tintoré, J., Orfilia, A., 2016. Wind influence on surface current variability in the Ibiza Channel from HF Radar. Ocean Dynamics.

Lellouche, J.M., Le Galloudec, O., Drévillon, M., Régnier, C., Greiner, E., Garric, G., Ferry, N., Desportes, C., Testut, C.E., Bricaud, C., Bourdallé-Badie, R., Tranchant, B., Benkiran, M., Drillet, Y., Daudin, A., De Nicola, C., 2012. Evaluation of real time and future global monitoring and forecasting systems at Mercator Océan. Ocean Science Discussion 9, 1123–1185.

Lipa, B., Nyden, B., Ullman, D.S., Terrill, E., 2006. SeaSonde radial velocities: derivation and internal consistency. IEEE Journal of Oceanic Engeneering 31 (4), 850–861.

Lipphardt, B.L., Kirwan, A.D., Grosch, C.E., Lewis, J.K., Paduan, J.D., 2000. Blending HF radar and model velocities in Monterey Bay through normal mode analysis. J. Geophys. Res. 105 (C2), 3425–3450.

Lorente, P., Piedracoba, S., Soto-Navarro, J., Alvarez-Fanjul, E., 2015. Evaluating the surface circulation in Ebro Delta (NE Spain) with quality controlled High-Frequency radar measurements. Ocean Sci. 11, 921–935.

Lorente, P., Piedracoba, S., Soto-Navarro, J., Ruiz, M.I., Alvarez-Fanjul, E., Montero, P., 2016. The High Frequency coastal radar network operated by Puertos del Estado (Spain): roadmap to a fully operational implementation. Journal of Oceanic Engineering 1–17 http://dx.doi.org/10.1109/JOE.2016.2539438 (accepted).

Madec, G., 2008. NEMO Ocean General Circulation Model, Reference Manual, Internal Report. LODYC/IPSL, Paris.

Maidana, M.A., Naudin, J.J., Espino, M., Garcia, M.A., Sanchez-Arcilla, A., 1999. Feasibility and usefulness of diagnostic calculations of the mean circulation in the vicinity of the Ebro mouth. Model tests against field data. Continental Shelf Research 22, 229–245.

Maraldi, C., Chanut, J., Levier, B., Ayoub, N., De Mey, P., Reffray, G., Lyard, F., Cailleau, S., Drévillon, M., Alvarez-Fanjul, E., Sotillo, M.G., Marsaleix, P., and the Mercator Team: NEMO on the shelf: assessment of the Iberia–Biscay–Ireland configuration. Ocean Science, Vol. 9, Issue 4, pp. 745–771, 2013.

Marmain, J., 2013. Coastal Circulation in the North Western Mediterranean: Current Measurements by HF Radar and Coupling With a Numerical Model Ph.D. dissertation Dept. Physics, University of Toulon.

Marmain, J., Molcard, A., Forget, P., Barth, A., 2014. Assimilation of HF radar surface currents to optimize forcing in the North Western Mediterranean sea. Nonlin. Processes Geophys. 21, 659–675.

Martin, M., 2011. In: Schiller, A., Brassington, G.B. (Eds.), Ocean forecasting systems – product evaluation and skill, Operational Oceanography in the 21st century. Springer, pp. 611–631 ISBN 978-94-007-0332-2.

Mihanović, H., Cosoli, S., Vilibić, I., Ivanković, D., Dadić, V., Gačić, M., 2011. Surface current patterns in the northern Adriatic extracted from high-frequency radar data using self-organizing map analysis. J. Geophys. Res. 116, C08033. http://dx.doi.org/10.1029/2011JC007104.

Muscarella, P.A., Barton, N.P., Lipphardt, B.L., Veron, D.E., Wonga, K.C., Kirwan, A.D.: Surface currents and winds at the Delaware Bay mouth, Continental Shelf Research, Volume 31, Issue 12, pp. 1282–1293. 2011.

Ngodock, H., Muscarella, P., Carrier, M., Souopgui, I., Smith, S., 2015. Assimilation of HF Radar Observations in the Chesapeake-Delaware Bay Region Using the Navy Coastal Ocean Model (NCOM) and the Four-Dimensional Variational (4DVAR) Method. Coastal Ocean Observing Systems, Elsevier, pp. 373–391 http://dx.doi.org/10.1016/B978-0-12-802022-7.00020-1 (Chapter 20).

North, G.R., Bell, T.L., Cahalan, R.F., Moeng, F.J., 1982. Sampling errors in the estimation of empirical orthogonal functions. Mon. Wea. Rev 110, 699–706.

O'Donncha, F., Hartnett, M., Nash, S., Ren, L., Ragnoli, E., 2015. Characterizing observed circulation patterns within a bay using HF radar and numerical model simulations. J. Mar. Syst. 142, 96–110.

Paduan, J.D., Shulman, I., 2004. CODAR data assimilation in the Monterey Bay area. Journal of Geophysical Research 109, C07S09 (http://dx.doi.org/10.1029/2003JC001949).

Paduan, J.D., Kim, K.C., Cook, M.S., Chavez, F.P., 2006. Calibration and validation of direction-finding High-Frequency radar ocean surface current observations. IEEE J. Ocean. Eng. 31 (4), 862–875.

Palanques, A., Guillen, J., 1998. Coastal changes in the Ebro Delta: natural and human factors. J. Coast. Conserv. 4, 17–26.

Palanques, A., Puig, P., Guillen, J., Jimenez, J., Gracia, V., Sanchez-Arcilla, A., Madsen, O., 2002. Near-bottom suspended sediment fluxes on the microtidal low-energy Ebro continental shelf (NW Mediterranean). Cont. Shelf Res. 22, 285–303.

Ren, L., Nash, S., Harnett, M., 2015. Observation and modelling of tide- and wind-induced surface currents in Galway Bay. Water Science and Engineering 8 (4), 345–352.

Rubio, A., Arnau, P.A., Espino, M., Flexas, M.M., Jorda, G., Salat, J., Puigdefàbregas, J., Sanchez-Arcilla., A., 2005. A field study of the behaviour of an anticyclonic eddy on the Catalan continental shelf (NW Mediterranean). Prog. Oceanogr. 66, 142–156.

Salat, J., Garcia, M.A., Cruzado, A., Palanques, A., Arín, L., Gomis, D., Guillen, J., de León, A., Puigdefàbregas, J., Sospedra, J., Velásquez, Z.R., 2002. Seasonal changes of water mass structure and shelf-slope exchanges at the Ebro Shelf (NW Mediterranean). Cont. Shelf Res. 22, 327–348.

Schaeffer, A., Garreau, P., Molcard, A., Fraunie, P., Seity, Y., 2011a. Influence of high-resolution wind forcing on hydrodynamic modeling of the Gulf of Lions. Ocean Dyn. 61, 1823–1844.

Schaeffer, A., Molcard, A., Forget, P., Fraunie, P., Garreau, P., 2011b. Generation mechanism for mesoscale eddies in the Gulf of Lions: radar observation and modeling. Ocean Dyn. 61, 1587–1609.

Shrira, V.I., Forget, P., 2015. On the nature of near-inertial oscillations in the uppermost part of the ocean and a possible route toward HF radar probing of stratification. J. Phys. Oceanogr. 45, 2660–2678.

Sotillo, M.G., Cailleau, S., Lorente, P., Levier, B., Aznar, R., Reffray, G., Amo-Baladrón, A., and Alvarez-Fanjul, E.: The MyOcean IBI Ocean forecast and reanalysis systems: operational products and roadmap to the future Copernicus service. Journal of Operational Oceanography, Vol. 8, Issue 1, pp. 1–18, 2015.

Stanev, E.V., Ziemer, F., Schultz-Stellenfleth, J., Seemann, J., Staneva, J., Gurgel, K.W., 2015. Blending surface currents from HF radar observations and numerical modelling: tidal hindcasts and forecasts. J. Atmos. Ocean. Technol. 32, 256–281.

Tonani, M., Pinardi, N., Fratianni, C., Pistoia, J., Dobricic, S., Pensieri, S., de Alfonso, M., Nittis, K., 2009. Mediterranean Forecasting System: forecast and analysis assessment through skill scores. Ocean Sci. 5, 649–660.

Warrick, J.A., DiGiacomo, P.M., Weisberg, S.B., Nezlin, N.P., Mengel, M.J., Jones, B.H., Ohlmann, J.C., Washburn, L., Terrill, E.J., Farnsworth, K.L., 2007. River plume patterns and dynamics within the Southern California Bight. Cont. Shelf Res. 7 (19), 2427–2448.

Wilkin, J.L., Hunter, E.J., 2013. An assessment of the skill of real-time models of Mid-Atlantic Bight continental shelf circulation. Journal of Geophysical Research, Oceans 118, 1–15.

Würtz, M., 2010. Mediterranean Pelagic habitat: Oceanographic and Biological Processes, an Overview. IUCN, Gland, Switzerland and Malaga, Spain ISBN: 9782831712420, 88 pages.

Yu, P., Kurapov, A.L., Egbert, G.D., Allen, J.S., Kosro, M., 2012. Variational assimilation of HF radar currents in a coastal ocean model off Oregon. Ocean Model. 49-50, 86–104.

Zelenke, B.C., Moline, M.A., Jones, B.H., Ramp, S.R., Crawford, G.B., Largier, J.L., Terrill, E.J., Garfield III, N., Paduan, J.D., Washburn, L., Others, 2009. Evaluating connectivity between marine protected areas using CODAR high-frequency radar. Proceeding at OCEANS MTS/IEEE, Biloxi, MS, pp. 1–10.